nature communications

Article

https://doi.org/10.1038/s41467-025-60454-5

Synthetic carbon-based lanthanide upconversion nanoparticles for enhanced photothermal therapy

Received: 12 January 2024

Accepted: 24 May 2025

Published online: 09 July 2025

Check for updates

Mei Yang[1,2,3,6] ✉, Yida Huang[4,6], Zhongxing Chen[1,2,3,6], Qianfang Ye[4,6], Zhenhai Zeng[1,2,3,6], Xinru You[5,6], Bijun Bao[4], Wenqian Xing[1,2,3], Nan Zhao[1,2,3], Zhilin Zou[4], Hongxian Pan[1,2,3], Xin Chen[1,2,3], Qingyi Gao[1,2,3], Tingting Chen[4], Shenrong Zhang[1,2,3], Aodong Chen[4], Yichen Xiao[1,2,3], Huilin Xu[4], Jiawei Li[4], Yongjiang Li[5], Na Kong[5], Wei Tao[5] ✉, Xingtao Zhou[1,2,3] ✉ & Jinhai Huang[1,2,3] ✉

Photothermal therapy (PTT), a vanguard strategy in cancer/ocular neovascularization treatment, has attracted considerable attention owing to its precision, controllability, high efficacy, and minimal side effects. Nevertheless, its inherent limitations necessitate innovative solutions. One promising strategy is to develop reagents with enhanced photothermal conversion efficiency under long-wavelength laser irradiation. Carbon nanomaterials, known for their broad absorption spectra, are currently hindered by single-wavelength lasers in clinical treatments. In this study, we address this limitation by coating mesoporous carbon nanomaterials (MCNs) with a lanthanide oxysulfide upconversion material ($Y_2O_2S:Yb^{3+},Er^{3+}$), converting 980 nm light into visible light. This advancement enhances the photothermal conversion efficiency of the produced MCNs/Ln/GD/FR nanocomposites from 59.48% to 82.86%. Furthermore, the incorporation of gambogic acid and doxorubicin intensifies the synergistic photothermal therapy effect. A dual stimuli-responsive hydrogel (PNIPAM) is employed to ensure controlled drug release and safe delivery to tumors. Evaluations demonstrate that the MCNs/Ln/GD/FR nanocomposites exhibit exceptional tumor targeting and evident photothermal synergistic therapy effects on both subcutaneous and ocular in situ melanoma tumors by activating tumor-suppressive signaling pathways while inhibiting proliferation and differentiation-related pathways. These findings might pave the way for the development of photothermal reagent and offer valuable insights for advancing therapeutic strategies.

In recent decades, considerable efforts have been dedicated to exploring innovative tumor/pathological neovascularization suppression techniques, encompassing a range of optical therapies such as photothermal therapy (PTT), photodynamic therapy, and photoacoustic therapy, as well as immunotherapy, radiotherapy, and gene therapy[1–7]. Each of these modalities presents unique advantages and challenges, underscoring the need for continuous optimization and broader implementation. Among these, PTT has emerged as a

A full list of affiliations appears at the end of the paper. ✉e-mail: meiyang@fudan.edu.cn; wtao@bwh.harvard.edu; xingtaozhou@fudan.edu.cn; jinhaihuang@fudan.edu.cn

cutting-edge treatment strategy, attracting considerable attention due to its precision, controllability, high efficacy, and minimal side effects[8,9]. However, PTT still faces some inherent challenges that require further addressal. The treatment of deep-seated cancers remains unsatisfactory due to the constraints of laser penetration, and the survival of residual tumor cells post-PTT may lead to metastasis[10,11]. Meanwhile, the efficacy of PTT can be compromised by the development of heat shock proteins, which act as protective shields for cancer cells[12,13]. Therefore, it is crucial to develop therapeutic agents that can reduce tumor cells' heat resistance and enhance lasers penetration depth to improve PTT efficacy and effectively eradicate tumor cells at lower laser intensities.

The application of nanocomposites (NPs) in the diagnosis and treatment of cancer or ocular neovascularization has received a lot of attention with the development of nanomaterials and nanotechnology. Kinds of functional drug molecules can be loaded through encapsulation, embedding, adsorption, or covalent coupling. Chemical modification can also enhance the selectivity and targeting of nanocomposites, improving drug uptake in affected tissues and reducing drug diffusion into normal tissue. Thus, developing nanocomposites with high photothermal conversion efficiency that can be irradiated with long-wavelength laser and used as carriers for functional drugs to amplify the photothermal synergistic therapy effect may be an effective approach to destroy target cells[14].

Mesoporous carbon nanomaterials (MCNs), a promising category of drug delivery nanocarriers, have been recognized as the next-generation platform for drug delivery and biomedical applications[15,16]. Their performances make them promising candidates for use in photothermal therapy, drug administration, and other fields[17,18]. Carbon nanomaterials exhibit strong absorption of near-infrared light, converting it into heat energy to induce cancer cells ablation[19]. They are recognized not only for their absorption in the near-infrared spectrum but also for their broad absorption band, which, when combined with single-wavelength lasers currently employed in clinical treatments, presents certain limitations. Specifically, the narrow wavelength range of single-wavelength lasers may not fully leverage the wide absorption band of carbon nanomaterials, thereby limiting their photothermal conversion efficiency and therapeutic efficacy. To enhance the photothermal conversion efficiency of the proposed nanocomposites under 980 nm laser irradiation, a layer of lanthanide oxysulfide up-conversion material (Y_2O_2S:Yb^{3+},Er^{3+}) was coated onto MCNs. This coating converts 980 nm light into visible light, effectively expanding the absorption wavelength range of the inner MCNs. The similar calcination preparation method of lanthanide oxysulfide with MCNs facilitates the synthesis of the proposed MCNs/Ln NPs[1,20,21].

Building on these foundations, highly photothermal conversion efficiency MCNs/Ln up-conversion nanocomposites are fabricated in this study. Gambogic acid (GA), a natural heat shock protein inhibitor that helps cells withstand heat-induced damage[22], and a broad-spectrum anticancer drug, doxorubicin (DOX), are loaded to enhance the photothermal synergistic therapy effect. Meanwhile, A dual stimuli-responsive hydrogel (PNIPAM) coating ensures controlled drug release and safe delivery to tumors[23,24]. In addition, the grafting of folic acid (FA) and cell membrane penetrating peptide R8 onto the nanocomposites further enhances their synergistic therapeutic effect by improving their efficient utilization in tumors. Figure 1 illustrates the schematic diagram of the synthesis of MCNs/Ln/GD/FR NPs and their application in photothermal synergistic therapy.

In this work, kinds of nanocomposites are synthesized and thoroughly characterized in terms of their morphology, influence factors, and photothermal conversion performances. Their biocompatibility and photothermal synergistic treatment effect are also extensively assessed in vitro and in vivo. In addition, subcutaneous and ocular in situ melanoma tumor models, long recognized as invaluable tools in fundamental research owing to their ability to mimic the disease's complex biology and clinical manifestations[25–27], are established to compare the efficacy of the photothermal synergistic therapy provided by these nanocomposites. The developed MCNs/Ln/GD/FR NPs display evident tumor (tumor cells) targeting and a pronounced photothermal synergistic therapy effect, which can significantly reduce the activity of OCM-1 cells and the growth of melanoma tumors. These findings not only offer insights on the exploration of low-temperature photothermal reagents but also provide a potential formulation to advancing photothermal therapy in anti-tumor, anti-angiogenesis, and antibacterial applications.

Results and discussion

Material characterization of MCNs/Ln NPs

To initiate the synthesis of MCNs/Ln NPs with MCNs as the core, a straightforward scheme is presented in Fig. 2A. The synthesis of MCNs involves a combination of solvothermal and hydrothermal methods to prepare their precursors (MCNs pre), followed by an annealing treatment. The size of the MCNs precursors can be modulated by adjusting the dropping rate of the Pluronic-127 aqueous solution (Supplementary Fig. 1), whereas the dropping rate of deionized water has a negligible effect (Supplementary Fig. 2). Then, a layer of lanthanide basic carbonate out-shell is coated onto the MCNs precursor (MCNs/Ln pre) using the solvothermal method. MCNs/Ln NPs are then obtained after calcination at an N_2/S atmosphere for 2 h. To determine the appropriate calcination temperature, thermogravimetric analysis (TGA) of the MCNs precursors and MCNs/Ln precursors was carried out in an N_2 atmosphere (Supplementary Fig. 3). Three distinct weight loss plateaus are observed for both samples. Around 35 % of the original sample remains for the MCNs/Ln precursors when the weight loss achieves equilibrium, which is higher than that of the MCNs precursors, where about 29 % of the original sample remains. Thus, three temperatures, including 700, 750 and 800 °C, were employed to anneal the precursors.

Then, SEM images of the MCNs pre, MCNs/Ln pre, and final MCNs/Ln NPs are presented in Fig. 2B. The diameter of the product increases sharply from 100 nm to 200 nm after being covered with the lanthanide basic carbonate shell. The thickness of the out-shell is approximately 50 nm. After the annealing treatment, the size of the products reduces to around 130 nm. The integrity of the nanocomposites can be disrupted as the calcination temperature increases. When the annealing temperature is raised to 800 °C, nearly no undamaged nanocomposites are observed (Supplementary Fig. 4). TEM and HRTEM images of the products further confirm the successful coating of the Y_2O_2S:Yb^{3+},Er^{3+} out-shell (Fig. 2C). TEM imaging of MCNs reveals that the sample is composed of 80 nm nanoparticles with numerous holes. The size increases from the initial 90 nm to about 130 nm when a layer of Y_2O_2S:Yb^{3+},Er^{3+} out-shell is coated (MCNs/Ln NPs). The HRTEM image with clear lattice fringes on the exterior further corroborates this conclusion. The lattice fringe with a *d*-spacing of 0.293 nm corresponds to the (101) plane of hexagonal Y_2O_2S.

X-ray diffraction patterns were further used to characterize the phase structures of the precursors and the MCNs/Ln NPs obtained at 700 °C. As shown in Fig. 2D, no noticeable diffraction peaks are observed in the MCNs and MCNs/Ln precursors, indicating poor crystalline. Strong and narrow diffraction peaks are found in the MCNs/Ln NPs, all peaks are consistent with those of the standard card (JCPDS#24-1424), indicating the formation of hexagonal Y_2O_2S after the annealing treatment. The structural alterations of the products were further verified by FTIR spectra (Supplementary Fig. 5). Compared to the MCNs precursors, a peak at 1525 cm^{-1} can be observed in the file of the MCNs/Ln precursors, with the peaks appeared at 948, 1238, and 1474 cm^{-1} in the FTIR spectrum of the MCNs precursors vanished, indicating the formation of different substances, which is ascribed to $Y(OH)CO_3$[28]. After being calcined, a strong absorption

https://doi.org/10.1038/s41467-025-60454-5

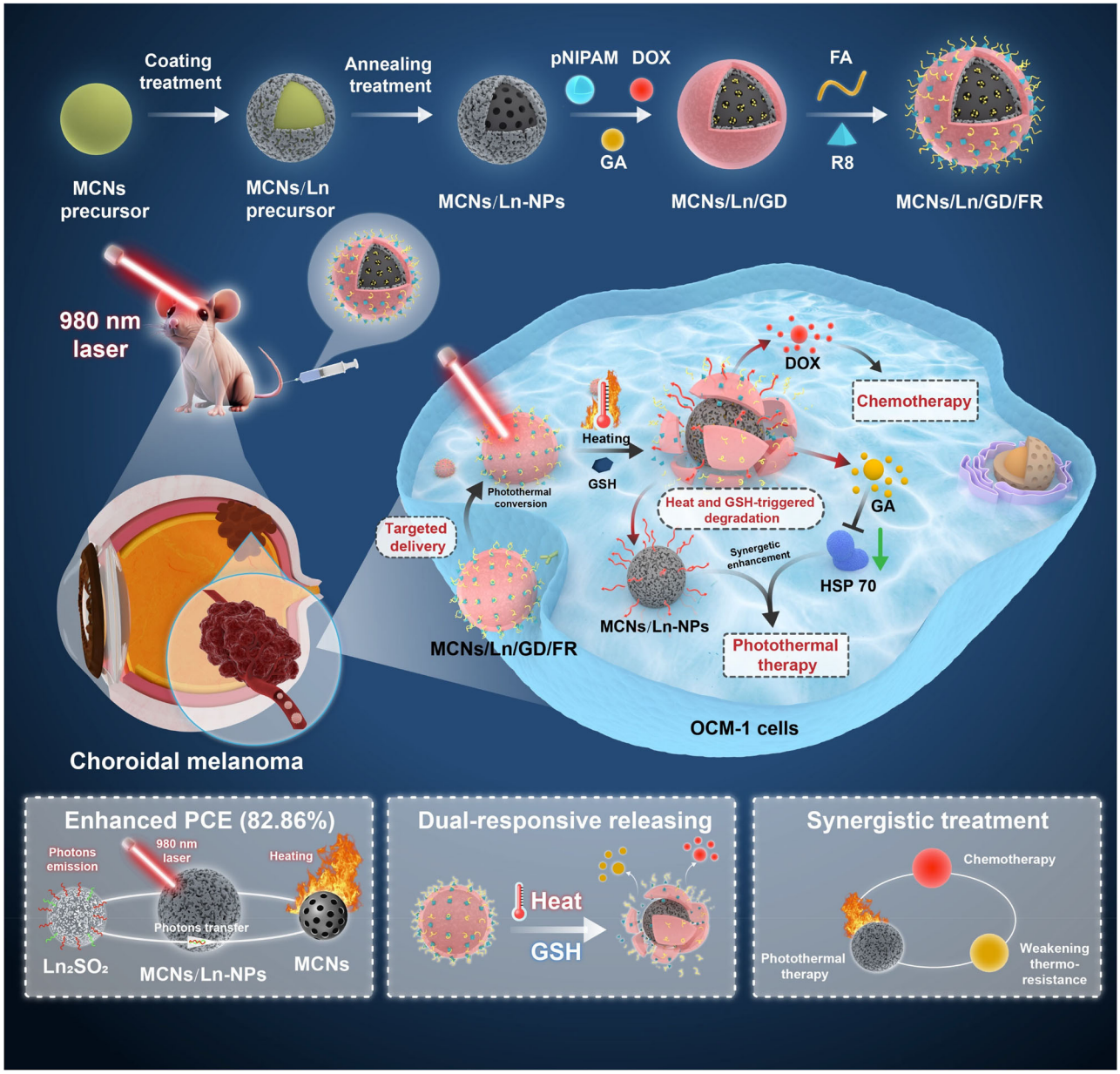

Fig. 1 | Schematic diagram. The synthesis of MCNs/Ln/GD/FR NPs and their application in photothermal synergistic therapy on melanoma.

peak, ascribed to the Ln-S bond, can be observed at 500 cm^{-1}, indicating the formation of oxysulfide in the final nanocomposites.

The specific surface area of MCNs and MCNs/Ln NPs was also compared using N_2 adsorption-desorption isotherms, as depicted in Fig. 2E. The samples exhibit VI-type isotherms with an H4-hysteresis loop, which is typical of activated carbon-type solids. The Brunauer–Emmett–Teller (BET) surface area of the MCNs is measured to be 523.31 $m^2 g^{-1}$, which dropped to 184.55 $m^2 g^{-1}$ after being coated in a layer of lanthanide oxysulfide due to its larger molar molecular weight. Holes with a diameter of around 3 nm remain, suggesting that the generated MCNs/Ln NPs could be an effective drug delivery carrier (inset in Fig. 2E). Meanwhile, the hydrophilic performance of the products was also investigated. Carbonaceous materials are known for their highly hydrophobic characteristics. When a shell of $Y_2O_2S:Ln^{3+}$ is coated, the contact angle of MCNs decreases from the initial 113.16° to 41.19°, close to that of water (36.63°), suggesting an obvious improvement of hydrophilicity. This is primarily due to the formation of a hydrophilic $Y_2O_2S:Ln^{3+}$ out-shell, whose contact angle is just approximately 27° (Supplementary Fig. 6). The enhanced hydrophilicity of the produced MCNs/Ln NPs benefits their use as a platform for drug loading and biomedical applications.

Furthermore, the impact of the coating of the $Y_2O_2S:Yb^{3+},Er^{3+}$ out-shell on the products' fluorescence performance was investigated. When exposed to a 980 nm laser, pure MCNs exhibit only a weak emission band at 830 nm. Conversely, the fluorescence spectra of $Y_2O_2S:Yb^{3+},Er^{3+}$ with different doping amounts of Yb^{3+} ions primarily consist of intense visible light emissions at 550 nm and 690 nm, along with a weaker near-infrared light at 820 nm. Notably, when doped with an optimized amount of 10% Yb^{3+} ions, the sample exhibits the strongest emission among the three tested samples (Supplementary Fig. 7). When a layer of $Y_2O_2S:Yb^{3+}$, Er^{3+} out-shell was wrapped around MCNs, the signal of $Y_2O_2S:Yb^{3+},Er^{3+}$ in the visible region decreases dramatically, while the near-infrared emission band (840 nm) increases weakly, indicating that the light emitted by $Y_2O_2S:Yb^{3+},Er^{3+}$ is primarily absorbed by the inner MCNs. Meanwhile, the intensity of the 840 nm emission band can be adjusted by varying the encapsulation quantities of the outer $Y_2O_2S:Yb^{3+},Er^{3+}$ up to 0.75 mmol. Further increasing the lanthanide nitrates to 1 mmol results in a decline in the 840 nm

https://doi.org/10.1038/s41467-025-60454-5

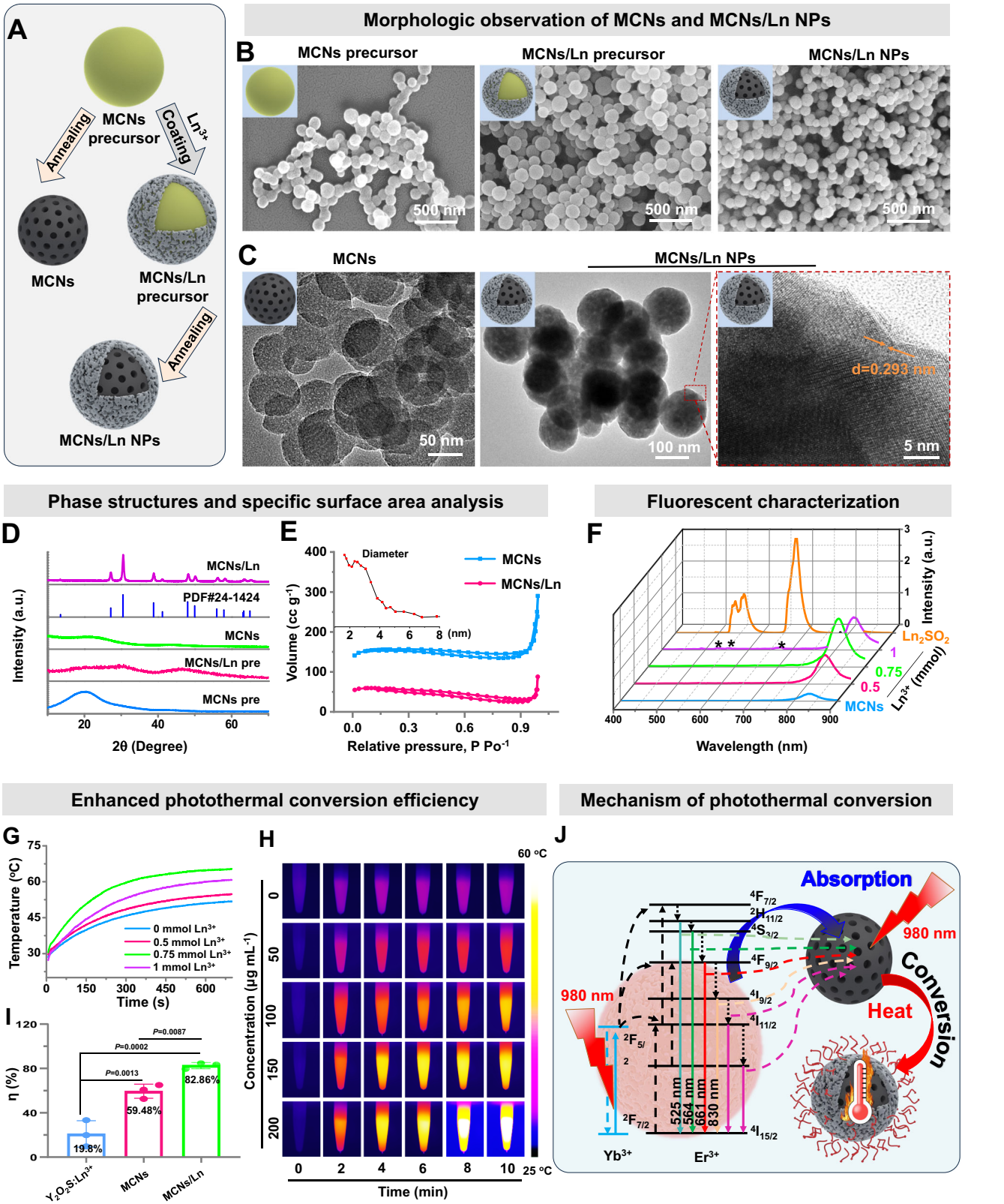

Fig. 2 | Material characterization of MCNs/Ln NPs. A A simple scheme of the synthesis of MCNs/Ln NPs. **B** SEM images of the MCNs precursors, MCNs/Ln precursors, and MCNs/Ln NPs treated at 700 °C in N_2/S atmosphere for 2 h. **C** TEM and HRTEM images of MCNs and MCNs/Ln NPs. **D** XRD patterns of the samples obtained at different conditions. **E** BET curves of the MCNs and MCNs/Ln NPs. **F** Emission spectra of the different samples under the irradiation of 980 nm laser. **G** The effect of lanthanide nitrate amounts on the effectiveness of the MCNs/Ln NPs' photothermal conversion. **H** The photothermal imaging of the nanocomposites with different irradiation times as well as concentrations. **I** The comparison of the photothermal conversion efficiency of Y_2O_2S:Yb^{3+},Er^{3+}, MCNs and MCNs/Ln NPs (0.75 mmol, data are presented as mean ± SD, $n = 3$ independent experiments, one-way ANOVA multiple comparison test, the absence of a P-value signifies no statistical significant difference between the groups ($P > 0.05$)). (**J**) The possible mechanism of the improvement of the photothermal conversion efficiency of the MCNs/Ln NPs.

emission band and the appearance of multiple weak emission bands at 550 nm and 690 nm (indicated using "*") of $Y_2O_2S:Yb^{3+},Er^{3+}$, ascribed to the limited light absorption capacity of the inner MCNs (Fig. 2F). The UV−vis−NIR absorption spectra of the different samples provide additional evidence that the presence of the MCNs core augments their capacity to absorb a wider spectrum of light wavelengths (Supplementary Fig. 8). The obvious photothermal conversion properties of the obtained MCNs/Ln nanocomposites, demonstrated subsequently, further confirmed that the light absorbed by MCNs is primarily converted into heat energy.

To assess the photothermal conversion properties of the synthesized nanocomposites, all samples were exposed to a 980 nm laser for 10 min at a distance of 3 cm from the optical fiber head to the center of the nanocomposite dispersion. Compared with MCNs, which exhibited a temperature increase from 29 to 51.5 °C within 10 min, the coating of a shell of $Y_2O_2S:Yb^{3+},Er^{3+}$ significantly enhanced the temperature elevation of the nanocomposites, especially for the sample prepared with 0.75 mmol of lanthanide nitrate, whose temperature increases from 29 to 65 °C (Fig. 2G). Aligning with the nanocomposites' fluorescence spectra (Fig. 2F), either increasing or decreasing the amount of lanthanide nitrate results in lower temperature increases. Meanwhile, the calcination temperature of the MCNs/Ln precursor influenced the photothermal conversion properties of the product. As shown in Supplementary Fig. 9A, the sample calcined at 700 °C displayed better photothermal conversion efficiency compared to those calcined at other temperatures (750 °C and 800 °C), whose decrease can be attributed to the loss of inner MCNs at higher calcination temperatures, as evidenced by SEM images (Supplementary Fig. 4). Furthermore, the laser power density also affected the final temperature of the nanocomposites. As the laser power density increased, the temperature of the nanocomposites clearly improved (Supplementary Fig. 9B). The influence of irradiation time and nanocomposites concentration on the mixture temperature was also carried out using photothermal imaging. The mixture temperature exhibited a clear dependency on both concentration and irradiation time under the same irradiation situation (Fig. 2H).

To gain a deeper understanding of the absorption characteristics of MCNs under multiple light sources, 660 nm and 980 nm lasers were employed to irradiate a 200 $\mu g\,mL^{-1}$ MCNs dispersion. As shown in Supplementary Fig. 10, the significant temperature increase observed with both lasers, compared to either laser alone, underscores the ability of MCNs to absorb and convert light from multiple wavelengths into thermal energy. Moreover, the photothermal conversion stability of the nanocomposites was evaluated by cycling the temperature between its maximum value and room temperature by turning the laser on and off. Five successive cycles were carried out, with the highest temperature in each cycle approaching 65 °C, indicating clear repeatability and photothermal conversion stability of the nanocomposites (Supplementary Fig. 11).

Furthermore, the photothermal conversion efficiency (η) of $Y_2O_2S:Yb^{3+},Er^{3+}$, MCNs and MCNs/Ln NPs (0.75 mmol) was compared. The η values were calculated from the temperature variation curves (Supplementary Fig. 12) and the linear relationship (Supplementary Fig. 13), according to the photothermal conversion equations (detailed in the Methods section -Synthesis of MCNs/Ln NPs)[29–32]. The η value for MCNs/Ln NPs was determined to be 82.86%, much higher than that of MCNs (59.48%) and $Y_2O_2S:Yb^{3+},Er^{3+}$ (19.8%), indicating an enhanced photothermal conversion efficiency for MCNs/Ln NPs (Fig. 2I).

To explore the distinct core-shell structure of MCNs/Ln nanocomposites that facilitates photothermal conversion, fluorescence spectroscopy was conducted on pure $Y_2O_2S:Yb^{3+},Er^{3+}$, mixtures of MCNs with $Y_2O_2S:Yb^{3+},Er^{3+}$, and MCNs/Ln nanocomposites. Despite similar solution colors, the mixture of MCNs and $Y_2O_2S:Yb^{3+},Er^{3+}$ exhibited a much stronger fluorescence signal compared to that of MCNs/Ln nanocomposites (Supplementary Fig. 14). This suggests that the seamless core-shell integration in the MCNs/Ln nanocomposites allows efficient photon capture by the inner MCNs from the outer $Y_2O_2S:Yb^{3+},Er^{3+}$ shell. In contrast, simple physical blending of MCNs with $Y_2O_2S:Yb^{3+},Er^{3+}$ does not facilitate effective photon capture, hindering subsequent thermal energy conversion.

Based on these findings, it is evident that the $Y_2O_2S:Yb^{3+},Er^{3+}$ out-shell on MCNs significantly enhances photothermal conversion efficiency. The potential mechanism behind this enhancement, illustrated in Fig. 2J, can be attributed to the meticulously designed core-shell structure of the MCNs/Ln nanocomposites. The MCNs, serving as the core, are engineered to efficiently absorb 980 nm light, a wavelength highly promising for laser-driven photothermal applications. This direct absorption markedly elevates the overall photothermal conversion efficiency of the MCNs/Ln system. The $Y_2O_2S:Yb^{3+},Er^{3+}$ out-shell encapsulating the MCNs also plays a crucial role. When exposed to a 980 nm laser, the electrons in the ground states of Yb^{3+} ions are excited and transition to their excited states. These excited electrons then transfer to the excited states of Er^{3+} ions, along with other electrons that are excited from the ground state of Er^{3+} ions. When these electrons relax back to the ground state of Er^{3+} ions, they emit light at various wavelengths, such as 550 nm and 690 nm. The inclusion of the MCNs core introduces an additional absorption process, where photons emitted from different excited states of Er^{3+} ions, and the initial 980 nm photons, are absorbed by the MCNs. This absorption process broadens the spectral range absorbed by the MCNs, further enhancing the overall absorbance and photothermal conversion efficiency. The seamless integration of the core-shell structure of the MCNs/Ln nanocomposites ensures the efficient capture of photons emitted by the $Y_2O_2S:Yb^{3+},Er^{3+}$ out-shell by the inner MCNs, ultimately contributing to the observed enhancement in photothermal conversion efficiency.

Material characterization of MCNs/Ln/GD/FR NPs

As illustrated in Fig. 3A, hydrophilic MCNs/Ln NPs, distinguished by their exceptional photothermal conversion performance, were further utilized as carriers. Subsequently, a series of experiments were conducted to optimize the synergistic therapeutic efficacy of the resultant product. These experiments included the physical adsorption of GA (termed MCNs/Ln/G), the encapsulation with a thermally and GSH-responsive PNIPAM hydrogel outer shell (yielding MCNs/Ln/G/pNIPAM NPs), the incorporation and entrapment of DOX within the unique grid structure of the pNIPAM hydrogel (denoted as MCNs/Ln/GD), and the covalent conjugation of FA and R8 via amide bond formation (identified as MCNs/Ln/GD/FR). Following these preparations, kinds of characterization techniques were employed to evaluate the diverse properties of the products.

Initially, the zeta potentials of the nanocomposites obtained at different stages were measured (Supplementary Fig. 15). The zeta potential values dropped from an initial 16.4 mV to 2.7 mV upon loading GA, and further fell to −17.3 mV when coated with the PNIPAM hydrogel. This value changed to 8.2 mV with the addition of DOX. The conjugation of FA and R8 on the surface cause the zeta potential to shift from −7.6 to −2.9 mV. The variations in zeta potential at each step further confirm the effective modification of the nanocomposites. In addition, the changes in hydrated particle size at several stages also verify the successful coating of $Y_2O_2S:Yb^{3+},Er^{3+}$and the PNIPAM hydrogel. The hydrated particle size increased from the initial 100 nm of MCNs to 200 nm for MCNs/Ln, and ultimately to 400 nm for MCNs/Ln/GD (Supplementary Fig. 16).

Comparing with the TEM image of MCNs/Ln NPs (Fig. 2C), a shell of amorphous material can be distinctly observed on the exterior of the $Y_2O_2S:Yb^{3+},Er^{3+}$ out-shell (Fig. 3A), which is ascribed to the PNIPAM hydrogel. Meanwhile, the drug loading and releasing properties of GA and DOX under different conditions were studied. The encapsulation efficiency (EE) and loading efficiency (LE) of DOX in the final

https://doi.org/10.1038/s41467-025-60454-5

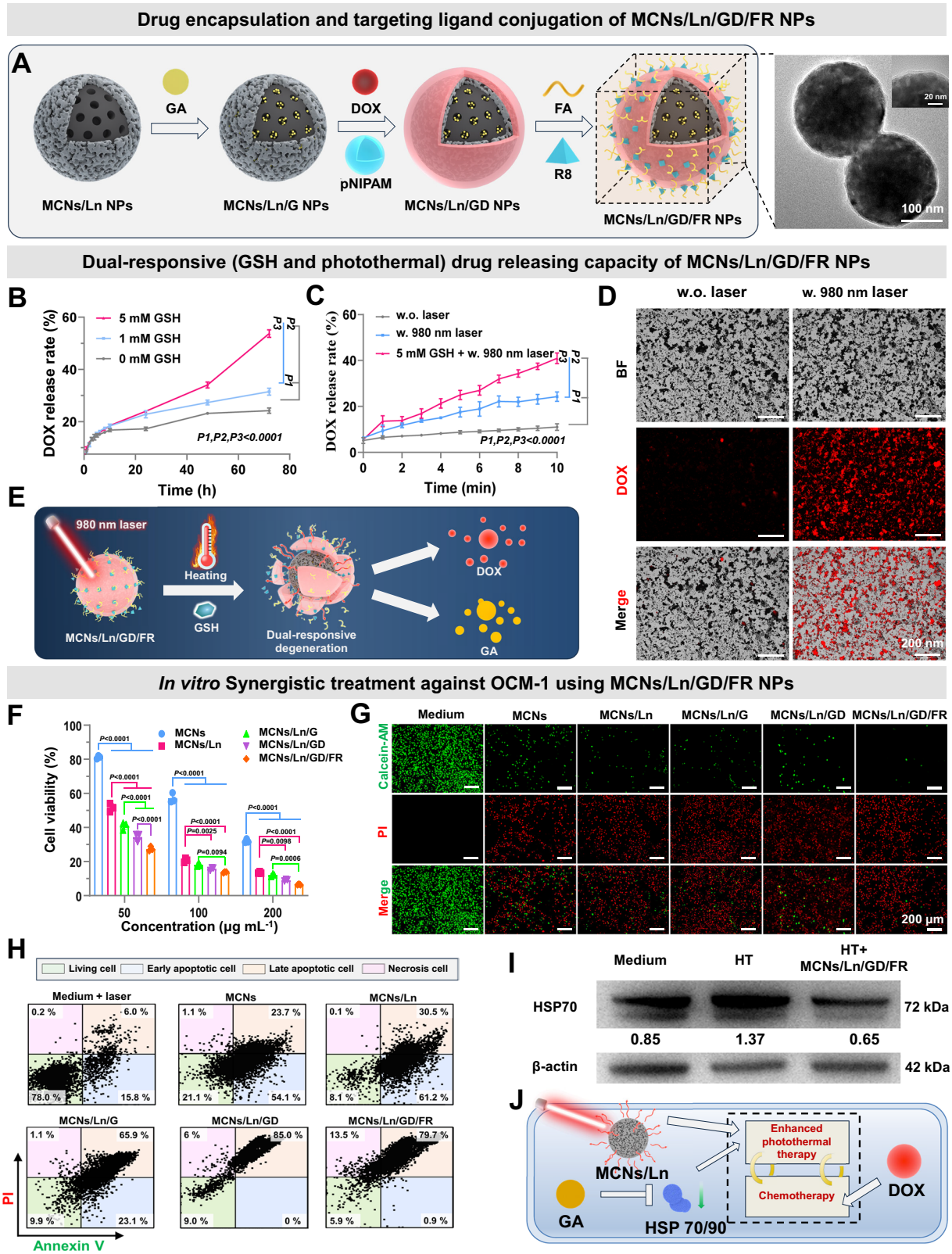

nanocomposites were higher than those of GA (Supplementary Fig. 17). About 58% of GA was released after 48 h of gentle shaking (Supplementary Fig. 18).

Due to the temperature and glutathione (GSH) stimuli-responsive properties of the PNIPAM hydrogel where DOX was entrapped, the release rate kinetics of DOX were further measured under different conditions. With the enhancement in GSH concentration, a greater amount of DOX was released over time, confirming that GSH facilitates the decomposition of the PNIPAM hydrogel. This is attributed to the presence of disulfide bonds (-S-S-) in the cross-linker hydrogel (Fig. 3B). Heating the nanocomposites also facilitated the release of DOX. Compared with the sample without heating, it took about 1 min for the decomposition of the PNIPAM hydrogel and the release of DOX, the addition of GSH in the solution accelerated the release of DOX

Fig. 3 | Characterization of MCNs/Ln/GD/FR NPs. A A simple scheme of the synthesis of MCNs/Ln/GD/FR NPs, and its TEM image. **B** The influence of GSH concentrations on the release of DOX (%) in MCNs/Ln/D NPs aqueous dispersion (Data are presented as mean ± SD, $n = 3$ independent experiments, two-way ANOVA multiple comparison test). **C** Release percentage of DOX (%) in MCNs/Ln/D NPs aqueous dispersion with or without irradiation, as well as the addition of GSH (Data are presented as mean ± SD, $n = 3$ independent experiments, two-way ANOVA multiple comparison test). **D** Fluorescence microscope images of the MCNs/Ln/D NPs aqueous dispersion with or without irradiation. **E** A simple release illusion of the temperature and GSH stimuli-responsive MCNs/Ln/GD/FR NPs. **F** PTT synthetic effect of the kinds of nanocomposites on OCM-1 cell viability under the irradiation of 980 nm laser (Data are presented as mean ± SD, $n = 3$ independent experiments, one-way ANOVA multiple comparison test, the absence of a P-value signifies no statistical significant difference between the groups ($P > 0.05$)). **G** Calcein-AM/PI double staining of OCM-1 cells incubated with various nanocomposites under 980 nm laser irradiation, with an untreated group as control (medium). **H** Flow-cytometric analysis of OCM-1 cells incubated with different nanocomposites under 980 nm laser irradiation, with a control group irradiated solely with 980 nm laser (medium). **I** The relative change of the expression of HSP70 protein under different conditions (β-actin was used as an internal control, HT: heat treatment). **J** The therapeutic effect of different components in MCNs/Ln/GD/FR NPs.

(Fig. 3C). Fluorescence microscope images of the MCNs/Ln/D aqueous dispersion with or without irradiation further confirmed the controllable release of DOX from the nanocomposites (Fig. 3D). These results imply that the obtained temperature and GSH stimuli-responsive MCNs/Ln/GD/FR NPs can be safely delivered in vivo before reaching the tumor or being heated (Fig. 3E).

Then, the cell biocompatibility of the various nanocomposites was investigated. The cell survival rate of ARPE-19 cells was initially evaluated after a 24 h incubation with several nanocomposites at different concentrations, including 50, 100, and 200 μg mL^{-1} (Supplementary Fig. 19A). The survival rates of ARPE-19 cells remained over 80% when the concentration of the nanocomposites reached 200 μg mL^{-1}, indicating obvious biocompatibility of the synthesized nanocomposites. The biocompatibility of the MCNs/Ln/GD/FR NPs was further assessed using three other cells types, including hRMEC, 293 T, and L929 cells, and compared after 24 h incubation. As shown in Supplementary Fig. 19B, when the concentration of MCNs/Ln/GD/FR NPs exceeded 200 μg mL^{-1}, the survival rates of the four types of cells remained above 80%. Further enhancing the concentration of the nanocomposites to 400 μg mL^{-1} resulted in similar outcomes, except for hRMEC cells, whose survival rates decreased to about 70%. All these data demonstrate that the generated MCNs/Ln/GD/FR NPs possess apparent biocompatibility.

In vitro Synergistic treatment of MCNs/Ln/GD/FR NPs

Prior to evaluating the PTT synthetic effect of the synthesized nanocomposites on cells, the photothermal effect of a pure 980 nm laser on the cells was investigated. OCM-1 cells were exposed to a 980 nm laser with varying power densities for 10 min at a distance of 3 cm (the distance from the optical fiber head to the middle of the medium). The cell survival rate was subsequently measured. According to Supplementary Fig. 20A, 85% of cells remained alive when the power density was increased to 280 mW cm^{-2}. The survival rate decreased drastically as the power density was further increased, demonstrating an enhanced photothermal inhibitory effect. An ARPE cell experiment further confirmed that a 280 mW cm^{-2} 980 nm laser is safe for ARPE cells (Supplementary Fig. 20B). Thus, a laser power density of 280 mW cm^{-2} was used in subsequent investigations.

Then, the photothermal impacts of different nanocomposites on OCM-1 cells under irradiation were evaluated. The concentrations of nanocomposites were set at 50, 100, and 200 μg mL^{-1}, respectively. As shown in Fig. 3F, the survival rate of OCM-1 cells dropped substantially as the nanocomposites concentration increased, indicating a concentration dependency of PTT synthetic effects. Meanwhile, the PTT synthetic effect among different nanocomposites at the same concentration was also compared. Take the concentration of 100 μg mL^{-1} as an example, approximately 60% of OCM-1 cells survived after being incubated with MCNs nanoparticles for 24 h. When a shell of $Y_2O_2S:Yb^{3+},Er^{3+}$ out-shell was coated, only about 20% of cells survived, highlighting the enhanced PTT efficacy of MCNs/Ln NPs. Furthermore, the loading of GA, DOX, coupled with the conjugation of FA and R8, amplified the nanocomposites' PTT synthetic therapeutic impact, with only about 13% of cells survived in the MCNs/Ln/GD/FR group. This value decreases to 6% when the concentration of the nanocomposites was increased to 200 μg mL^{-1}. Meanwhile, the decrease in cell survival rates for different groups also verify the successful modification of the MCNs/Ln NPs.

Calcein-AM/PI double staining was also used to evaluate the PTT synthetic effect of the produced nanocomposites on OCM-1 cells. The nanocomposites were concentrated at 200 μg mL^{-1}, and the irradiation time of a 280 mW cm^{-2} 980 nm laser at 3 cm was set to 10 min with the medium group untreated. As illustrated in Fig. 3G, the quantity of living cells (green fluorescence) in the visual field decreases steadily with the modification progress of the nanocomposites. Meanwhile, the number of dead cells (red fluorescence) increased noticeably with the coating of $Y_2O_2S:Yb^{3+}$, Er^{3+}, the loading of GA, DOX, and the connection of FA and R8. Only a few living cells could be seen in the MCNs/Ln/GD/FR group, suggesting its outstanding PTT synthetic effect on OCM-1 cells.

The cell apoptosis of OCM-1 cells treated with different samples was further examined using flow cytometry to precisely depict the PTT synergistic impact of the different nanocomposites. The nanocomposites were concentrated at 200 μg mL^{-1}, and the irradiation time of a 280 mW cm^{-2} 980 nm laser at 3 cm was set to 10 min for all groups. The percentage of live cells decreased considerably with the progress of the modification (Fig. 3H). Compared to MCNs (21.1%), the percentage of live cells reduces to 8.14% when a layer of $Y_2O_2S:Yb^{3+},Er^{3+}$ out-shell was coated, suggesting the greatly improved PTT impact of MCNs/Ln NPs. The percentage of cells in the late stage of apoptosis increases considerably with the addition of GA and DOX. The modification of FA and R8 can reduce the percentage of live cells to 5.9%, much lower than that in other groups, further demonstrating the improved tumor targeting after modification.

Meanwhile, the expression of heat shock protein (HSP)-associated proteins in OCM-1 cells under heating treatment was studied using western blot analysis (Fig. 3I, J and Supplementary Fig. 21, 22). The level of HSP70 decreased from 1.37 to 0.65 under the intervention of MCNs/Ln/GD/FR NPs and laser irradiation, suggesting that the administration of GA can downregulate HSP70 expression in these cells, which facilitates the apoptosis of OCM-1 cells by minimizing their resistance and enhancing anticancer effects during heating treatment. In further photothermal inhibition experiments on HSP70-knockdown OCM-1 cells achieved via small interferencing RNA (SiRNA), an enhanced sensitivity to photothermal therapy was observed. This was evident when the cells were treated with 100 μg mL^{-1} MCNs/Ln nanocomposites and subjected to laser irradiation or exposed directly to a 45 °C incubation environment, resulting in a significant decrease in cell viability compared to other groups (Supplementary Fig. 22). This provides further evidence supporting the effectiveness of photothermal synergistic therapy.

Increased uptake of MCNs/Ln/GD/FR NPs in vitro *and* in vivo

The tumor (tumor cell) targeting efficacy of MCNs/Ln/GD/FR NPs was investigated both in vitro *and* in vivo. Given that OCM-1 cells possess a higher density of folate targeting receptors compared to ARPE-19 cells[33,34], MCNs/Ln/GD/FR NPs conjugated with FA are expected to

https://doi.org/10.1038/s41467-025-60454-5

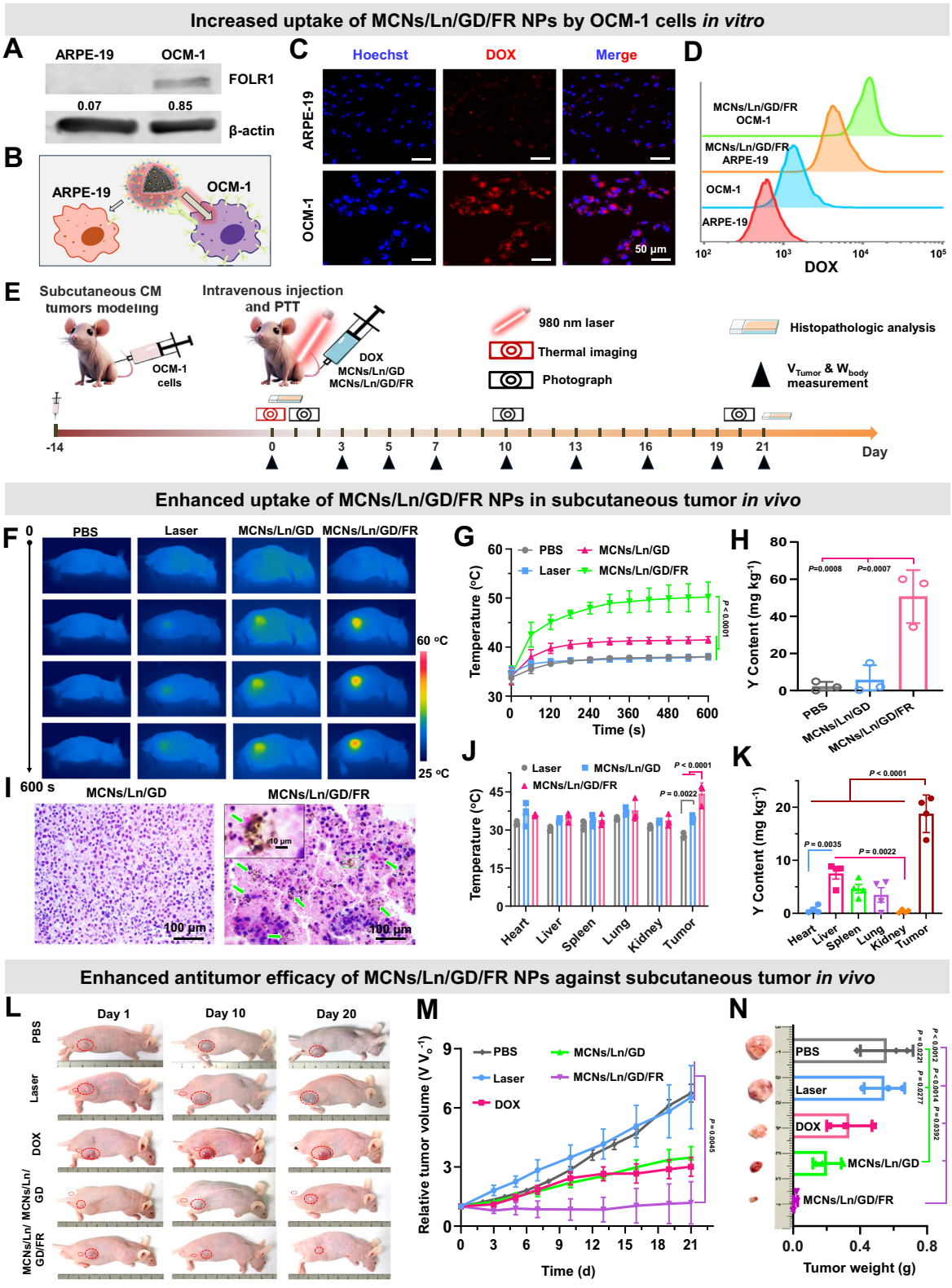

more effectively target OCM-1 cells than ARPE-19 cells under identical conditions (Supplementary Fig. 23 and Fig. 4A, B). Leveraging the red fluorescence signal of DOX, 200 μg mL^{-1} MCNs/Ln/D/FR NPs were co-cultured with ARPE-19 and OCM-1 cells for 6 h and subsequently examined using a confocal microscope. As depicted in Fig. 4C, with the cell nucleus stained by DAPI (blue), a greater intensity of red DOX fluorescence signals was observed in OCM-1 cells compared to ARPE-19 cells, indicating a higher uptake of nanocomposites by OCM-1 cells. The fluorescence quantitative analysis further confirmed that OCM-1 cells exhibited a higher DOX concentration (Fig. 4D), indicating that MCNs/Ln/D/FR NPs possess a superior targeting potential for OCM-1 tumor cells. Besides, the tumor cell targeting of MCNs/Ln/D and MCNs/Ln/D/FR NPs to OCM-1 cells was observed using confocal microscopy. After being

Fig. 4 | The tumor (tumor cells) targeting and antitumor efficacy of MCNs/Ln/GD/FR NPs against subcutaneous melanoma. A The expression of folate receptors in OCM-1 and ARPE-19 through Western Blot (n = 3 independent experiments). **B** one scheme of the expression of folate receptors in OCM-1 and ARPE-19. **C** The confocal microscope luminescent imaging of ARPE-19 and OCM-1 cells co-cultured with 200 μg mL^{-1} MCNs/Ln/D/FR NPs for 6 h. **D** Fluorescence quantitative analysis diagram of cells co-cultured with 200 μg mL^{-1} MCNs/Ln/D/FR NPs. **E** A simple scheme illustrating the procedures of subcutaneous melanoma modeling and intervention. **F** Thermal imaging photos of nude mice injected with different samples through the tail vein with the irradiation of 980 nm laser ($n = 5$ mice). **G** Temperature curves of the tumor of different groups (Data are presented as mean ± SD, $n = 5$ mice (for Laser group, $n = 4$ mice), one-way ANOVA multiple comparison test, the absence of a P-value signifies no statistical significant difference between the groups ($P > 0.05$)). **H** The Y content in the tumors of different groups (Data are presented as mean ± SD, $n = 3$ mice, one-way ANOVA multiple comparison test, the absence of a P-value signifies no statistical significant difference between the groups ($P > 0.05$)). **I** H&E staining of the tumor tissues of MCNs/Ln/GD and MCNs/Ln/GD/FR groups ($n = 3$ mice). **J** Histogram of the temperature of different organ tissues obtained from different groups (Data are presented as mean ± SD, $n = 3$ mice, one-way ANOVA multiple comparison test, the absence of a P-value signifies no statistical significant difference between the groups ($P > 0.05$)). **K** The Y content in different organ tissues in MCNs/Ln/GD/FR groups (Data are presented as mean ± SD, $n = 4$ mice, one-way ANOVA multiple comparison test, the absence of a P-value signifies no statistical significant difference between the groups ($P > 0.05$)). **L** Photos of nude mice in different time intervals after treatment. **M** Tumor volume change curves of the different groups (Data are presented as mean ± SD, $n = 3$ mice, one-way ANOVA multiple comparison test, the absence of a P-value signifies no statistical significant difference between the groups ($P > 0.05$)). **N** Photograph and qualities of the resected tumor tissues in different groups (Data are presented as mean ± SD, $n = 3$ mice, one-way ANOVA multiple comparison test, the absence of a P-value signifies no statistical significant difference between the groups ($P > 0.05$)).

co-cultured with 200 μg mL^{-1} MCNs/Ln/D and MCNs/Ln/D/FR NPs for 6 h, a greater accumulation of MCNs/Ln/D/FR NPs was observed surrounding the OCM-1 cell compared to MCNs/Ln/D NPs, which were evenly dispersed in the medium (Supplementary Fig. 24), suggesting that MCNs/Ln/D/FR NPs had a stronger targeting capacity for the OCM-1 tumor cell.

The tumor-targeting effect of MCNs/Ln/GD/FR NPs was also investigated in nude mice. A schematic illustration outlines the procedures for creating subcutaneous melanoma modeling and intervention (Fig. 4E). Four groups, including PBS, Laser, MCNs/Ln/GD and MCNs/Ln/GD/FR, were established. Mice were injected with 200 μL of PBS, MCNs/Ln/GD (2 mg kg^{-1}), and MCNs/Ln/GD/FR (2 mg kg^{-1}) PBS dispersion via the caudal vein. After 4 h post-injection, the mice were sedated, and various measurements were conducted. Initially, the tumor color in the four groups was compared. The tumor color in the MCNs/Ln/GD/FR group appeared much darker than that in the other groups (Supplementary Fig. 25A), indicating a greater accumulation of MCNs/Ln/GD/FR NPs at the tumor site. Simultaneously, the tumor sites were irradiated with a 280 mW cm^{-2} 980 nm laser, and thermal imaging photographs of the tumor sites were captured. A notably higher tumor temperature was observed in mice injected with MCNs/Ln/GD/FR NPs, indicating a greater integration of nanocomposites in the tumor tissue (Supplementary Fig. 25B). The thermal imaging images and temperature variation curves obtained at different time intervals also demonstrated that the tumor temperature in the MCNs/Ln/GD/FR group was much higher than that in the other three groups for the same irradiation duration (Fig. 4F, G). Inductively Coupled Plasma (ICP) analysis of Y content in tumor tissue from different groups further confirmed that more MCNs/Ln/GD/FR NPs accumulated in the tumor tissue (Fig. 4H). The comparison of HE images of tumor tissues in the MCNs/Ln/GD and MCNs/Ln/GD/FR groups also supported this conclusion, with more MCNs/Ln/GD/FR black nanocomposites, evident cells necrosis, and inflammatory cell infiltration observed in the tumor tissue of MCNs/Ln/GD/FR group (Fig. 4I and Supplementary Fig. 26 (enlarged images), green narrows indicating the nanocomposites).

Thermal imaging photographs and ICP analysis of Y content in heart, liver, spleen, lung, kidney, and tumor tissues of nude mice in the Laser, MCNs/Ln/GD and MCNs/Ln/GD/FR groups were also performed under irradiation. Compared to other tissues in the MCNs/Ln/GD/FR group or tumor tissues in other groups, the local temperature of tumor tissues in the MCNs/Ln/GD/FR group is considerably higher (Supplementary Fig. 27 and Fig. 4J). ICP analysis of Y content in different tissues further verified that more MCNs/Ln/GD/FR NPs accumulated in tumors, implying that the designed MCNs/Ln/GD/FR NPs exhibited distinct tumor targeting capacity while remaining reasonably safe for other tissues (Fig. 4K).

Enhanced antitumor efficacy of MCNs/Ln/GD/FR NPs against subcutaneous tumor in vivo

To assess the synergistic therapeutic effect of MCNs/Ln/GD/FR NPs on tumors in vivo, two types of melanoma models were established, including subcutaneous tumors and in situ ocular tumors, through localized injection of OCM-1 cells. For the treatment of subcutaneous melanoma, variations of body weight and tumor volume in nude mice, along with photographic records, were documented. Throughout the treatment period, the body weight of the nude mice remained stable, indicating evident biocompatibility of the proposed nanocomposites (Supplementary Fig. 28). In contrast, tumor volume varied substantially across different groups. Unlike the tumor volumes in the PBS, Laser, DOX, and MCNs/Ln/GD groups, which increased over time, the volume values in the MCNs/Ln/GD/FR group decreased gradually. After 21 days of treatment, the tumors of some mice disappeared, demonstrating the obvious tumor suppressive effect of the MCNs/Ln/GD/FR NPs (Fig. 4L, M). Photographs of the tumors during the treatment process and after removal from the mice further supported these findings (Fig. 4L, N). Histological examinations using hematoxylin and eosin (H&E) staining were conducted on the heart, liver, spleen, lung, and kidney tissues of the nude mice across all five groups. No visible harm was observed in these organs. Hepatocytes in liver samples appeared normal, no pulmonary fibrosis was found in lung samples, the glomerulus structure in kidney sections was visible, and no necrosis was evident in the histological samples. These results indicate that the use of MCNs/Ln/GD/FR NPs did not induce any clear pathological changes in the heart, liver, spleen, lung, or kidney (Supplementary Fig. 29).

Antitumor efficacy of MCNs/Ln/GD/FR NPs against in situ ocular melanoma

To evaluate the therapeutic effect of MCNs/Ln/GD/FR NPs on in situ ocular tumors, an ocular melanoma model was established through subretinal injection of OCM-1 cells into the eyes. The firefly luciferase gene (Luc) was introduced into OCM-1 cells for in vivo monitoring of tumor size. Figure 5A provides a schematic illustration of the melanoma in situ modeling and intervention process.

Prior to treatment, an evaluation was conducted to assess the ocular tumor targeting capability of the constructed MCNs/Ln/GD/FR nanocomposites. The experiment involved four groups: PBS, DOX, MCNs/Ln/GD, MCNs/Ln/GD/FR, all administered via tail intravenous injection. 6-hour post-administration, the eyeballs of the experimental animals in each group, along with various organs from the MCNs/Ln/GD/FR group, were collected. The distribution of the material was evaluated using the fluorescent properties of DOX. The results, as depicted in Supplementary Figs. 30 and 31, demonstrate that the fluorescence intensity of DOX in the eyeballs of the MCNs/Ln/GD/FR

https://doi.org/10.1038/s41467-025-60454-5

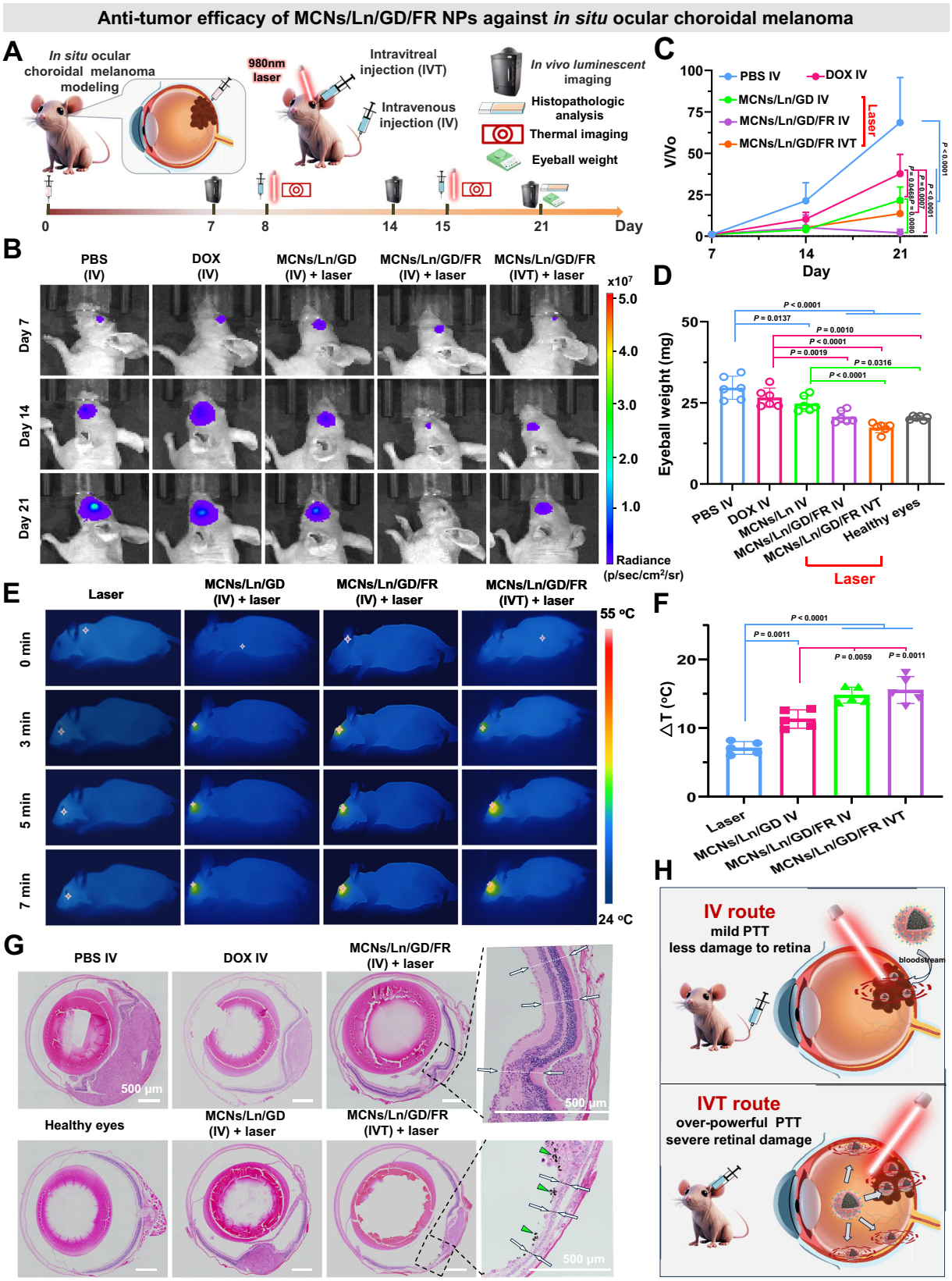

group was significantly higher compared to the other experimental groups. This finding suggests that the constructed MCNs/Ln/GD/FR nanocomposites can effectively cross the blood-ocular barrier and target ocular tissues, even when administered via tail intravenous injection, enabling targeted delivered to ocular tumor (Supplementary Fig. 30). When comparing the distribution of the MCNs/Ln/GD/FR nanocomposites in other organ tissues, it is observed that, after a 6-hour period of blood circulation, the nanocomposites are primarily distributed in the eyes and two major metabolic organs, namely the liver and kidneys, with minimal impact on other organs (Supplementary Fig. 31). These results indicate that the nanocomposites exhibit a favorable safety profile and ocular tumor-targeting capability,

Fig. 5 | Synergistic treatment effect of MCNs/Ln/GD/FR NPs in melanoma in situ. A A simple scheme illustrating the procedures of melanoma in situ modeling and intervention. **B** In vivo tumor bioluminescence images of the eyes in OCM-1-Luc tumor-bearing BALB/c nude mice with different treatments ($n = 5$ mice). **C** The corresponding relative tumor luminescence variation in different groups (Data are presented as mean ± SD, $n = 5$ mice, one-way ANOVA multiple comparison test, the absence of a *P*-value signifies no statistical significant difference between the groups ($P > 0.05$)). **D** The eyeball weight of different groups (Data are presented as mean ± SD, $n = 6$ mice, one-way ANOVA multiple comparison test, the absence of a *P*-value signifies no statistical significant difference between the groups ($P > 0.05$). **E** Thermal imaging photos of nude mice with different treatments under the irradiation of 980 nm laser ($n = 5$ mice). **F** Eye temperature variation of the nude mice for the different groups under the irradiation of 980 nm laser (Data are presented as mean ± SD, $n = 5$ mice, one-way ANOVA multiple comparison test, the absence of a *P*-value signifies no statistical significant difference between the groups ($P > 0.05$)). **G** H&E staining on the eyes in different groups ($n = 3$ mice). **H** Scheme of the potential effects of MCNs/Ln/GD/FR NPs in melanoma in situ using two administration methods.

establishing a solid foundation for further treatment of in situ ocular tumors.

In this study, two injection methods were compared: intravitreal injection (IVT) and intravenous injection (IV). In vivo optical imaging, variations of eyeball weight, and temperature changes in the eye under irradiation were recorded. After the administration of D-Luciferin Sodium Salt (Solarbio) for 15 min, the normalized eye fluorescence intensity of different groups was compared. The tumor bioluminescence intensity in the MCNs/Ln/GD/FR (IV) group was significantly lower than that in other groups, indicating a distinct inhibition effect of the nanocomposites (Fig. 5B). To quantitatively evaluate the tumor growth process, the bioluminescence intensity of tumors on the day before treatment (7^{th} day) was used as a baseline, and the tumor bioluminescence intensity curves of the different groups were recorded over the treatment period (Fig. 5C). Compared with the PBS and DOX groups, the bioluminescence intensity variation trend of the MCNs/Ln/GD and MCNs/Ln/GD/FR groups was much slower. Notably, in the group treated with MCNs/Ln/GD/FR(IV), the average bioluminescence intensity value on the 21^{st} day was close to the baseline, significantly lower than that of the other groups, indicating effectively inhibited.

Meanwhile, the eyeballs were carefully collected and weighed on the 21^{st} day. Among the different groups, only the average eyeball weight in the MCNs/Ln/GD/FR(IV) and MCNs/Ln/GD/FR(IVT) groups was comparable to that of the healthy eyes group, with no significant difference (Fig. 5D), indicating the clear synergistic treatment effect of the nanocomposites. The modification with FA and R8 appears to improve therapy efficiency. During the treatment, the temperature variation of the eye under irradiation was also recorded using an infrared thermal imager. Compared to the MCNs/Ln/GD(IV) group, a significantly higher variation in eye temperature was observed in the MCNs/Ln/GD/FR(IV) group, with statistical significance ($P = 0.0011$). This variation is nearly comparable to that of the MCNs/Ln/GD/FR(IVT) group, further suggesting that the linkage of FA and R8 enhances the curative effect by improving tumor targeting, even when administered via tail intravenous injection (Fig. 5E, F). Furthermore, the Kaplan–Meier survival curve demonstrated that photothermal treatment using MCNs/Ln/GD/FR(IV) facilitated the most comprehensive tumor resection and enhanced the overall survival rate of mice compared to the other groups (Supplementary Fig. 32).

Next, H&E staining was performed on the eyes of different groups. Obvious distortion of the eye was observed in the PBS group due to the extensive proliferation of OCM-1 cells. The tumors in the DOX(IV) and MCNs/Ln/GD(IV) groups were smaller but not as small as those in the MCNs/Ln/GD/FR groups using both injection strategies. However, retinal detachment and a smaller vitreous body were observed in the MCNs/Ln/GD/FR(IVT) group, which could be attributed to the higher eye temperature under irradiation. In contrast, almost no retinal detachment or vitreous body shrinkage was observed in the eyes of the MCNs/Ln/GD/FR(IV) group (Fig. 5G). Combined with the above evaluation results, this mild PTT treatment appears to be healthier (Fig. 5H).

In addition, fluorescent staining was conducted on the treated eyes in the MCNs/Ln/GD/FR(IV) groups to investigate the variation of associated heat shock proteins in vivo. As shown in Supplementary Fig. 33 and Supplementary Fig. 34, compared to untreated tumor tissues, the observed decrease in the levels of heat shock proteins, such as HSP70 and HSP90, in the treated tumor tissues further confirms that the application of MCNs/Ln/GD/FR NPs can effectively reduce the production of heat shock proteins within tumor tissues, ultimately contributing to the enhancement of the photothermal effect.

In vivo safety evaluation of MCNs/Ln/GD/FR NPs

The potential toxicity of the proposed MCNs/Ln/GD/FR NPs was further assessed following PTT treatment. Assessments included hemolysis analysis, H&E staining of organs, ICP analysis of Y content, and biochemical blood analysis in the mice administered with MCNs/Ln/GD/FR NPs via tail intravenous injection over a one-month period. The hemolysis rate of red blood cells was approximately 1.33% when the concentration of MCNs/Ln/GD/FR NPs reached 200 μg mL^{-1}, indicating that the MCNs/Ln/GD/FR NPs had no noticeable impact on immune regulation or heme response and demonstrated good blood biocompatibility (Fig. 6A and Supplementary Fig. 35). H&E staining of various tissues revealed no pathological changes in the heart, liver, spleen, lung, or kidney over the treatment duration (Fig. 6B). The ICP analysis of Y content in different tissues showed a substantial decrease with prolonged treatment (Fig. 6C), comparing to initial Y levels (Fig. 4K). Specifically, Y content in the liver reduced from an initial 20 mg kg^{-1} to around 2.4 mg kg^{-1} after one month of treatment, indicating that the synthesized MCNs/Ln/GD/FR NPs are metabolizable. Concurrently, blood samples were collected from nude mice on the 15^{th} and 30^{th} day following PTT treatment with MCNs/Ln/GD/FR NPs administered via tail intravenous injection ($n = 5$), with mice injected with PBS serving as the control group. Blood biochemical tests were then performed. Figure 6d illustrates the findings, showing that only aspartate aminotransferase (AST) levels remained slightly higher than the control group on both days 15 and 30, yet within an acceptable range. Liver and renal markers, as well as other parameters, were all within normal limits. These findings suggest that there was no significant inflammation or infection in the mice treated with the synthesized MCNs/Ln/GD/FR NPs as PTT agents.

In addition, the safety of MCNs/Ln/GD/FR NPs in ocular tissues was further conducted using TUNEL staining in the MCNs/Ln/GD/FR(IV) and MCNs/Ln/GD/FR(IVT) groups to investigate changes in apoptotic proteins. As depicted in Fig. 6E, TUNEL staining revealed obvious green staining in the tumor regions of both experimental groups, indicating a substantial presence of apoptotic cells in the tumor tissues and validating the effectiveness of the nanocomposites. However, notable differences were observed in the non-tumor regions between the two groups. Specifically, the non-tumor area in the MCNs/Ln/GD/FR(IVT) group also exhibited bright green fluorescence, suggesting, along with HE staining results, that the dispersion of materials in other ocular regions (such as the retinal region) could cause substantial damage during photothermal treatment. Conversely, the MCNs/Ln/GD/FR(IV) group showed reduced green fluorescence in the non-tumor area, indicating minimal tissue damage. This is attributed to the nanocomposites's ability to accumulate directly at the tumor site after passing through the blood-eye barrier when administered via

https://doi.org/10.1038/s41467-025-60454-5

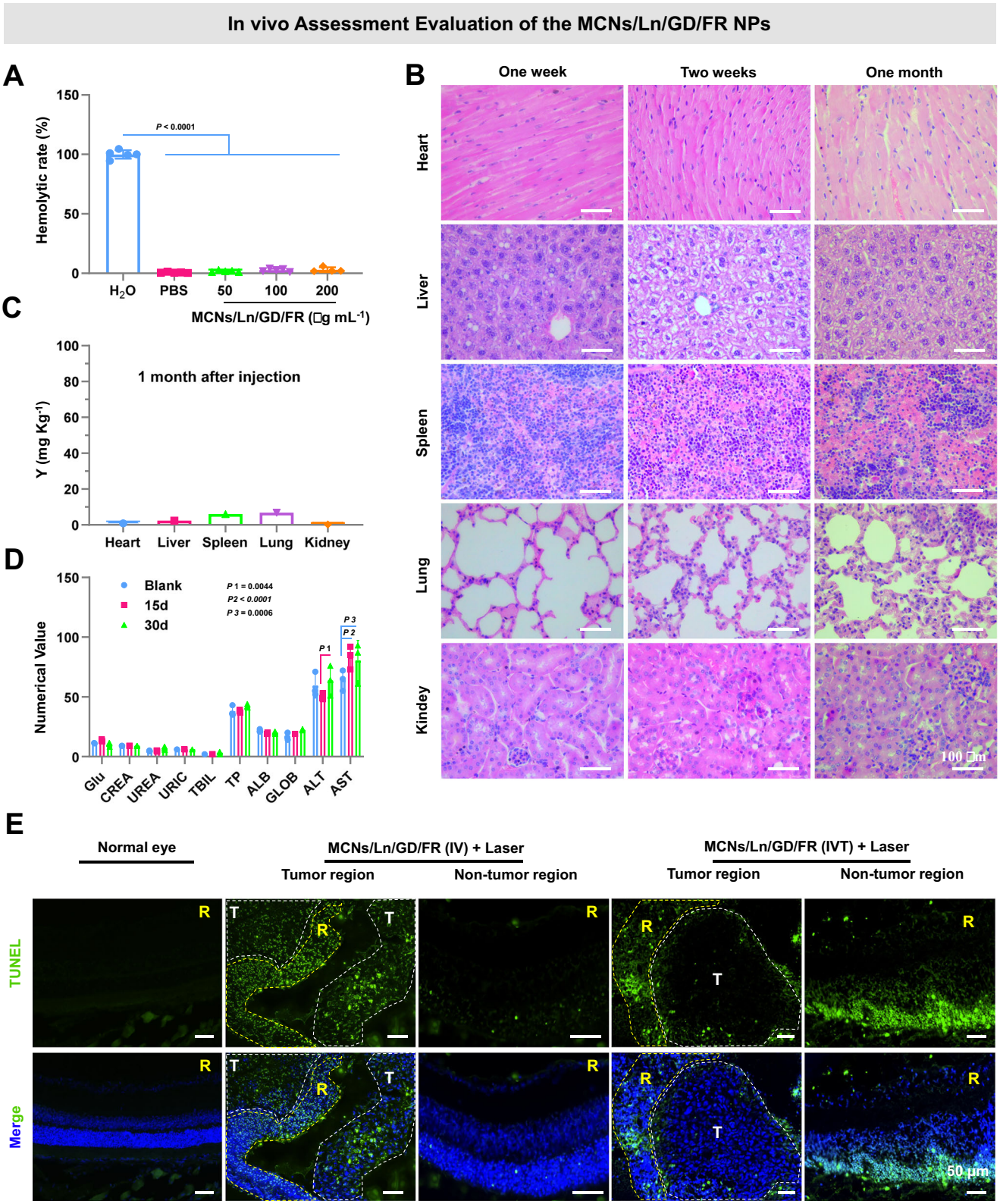

Fig. 6 | In vivo safety evaluation after PPT treatment. A Hemolysis experiment of MCNs/Ln/GD/FR NPs with different concentrations (Data are presented as mean ± SD, $n = 5$ (for 200 group, $n = 4$) independent experiments, one-way ANOVA multiple comparison test, the absence of a P-value signifies no statistical significant difference between the groups ($P > 0.05$)). **B** H&E staining of the organs from nude mice injected with MCNs/Ln/GD/FR NPs in different treatment periods ($n = 3$ mice, one week, two weeks, one month). **C** The ICP results of Y content in different organs after one-month treatment (The same organs of 5 mice were homogenized together to make one sample). **D** Serum biochemistry results of the blood obtained from nude mice after intravenous administration of MCNs/Ln/GD/FR NPs for 0, 15, and 30 ds, with mice injected with PBS as the Blank group (Glu: blood sugar. CREA: creatinine. Urea: UREA. URIC: URIC acid. TBIL: total bilirubin. TP: total protein. ALB: albumin. GLOB: globulin. ALT: alanine transaminase. AST: glutamic-oxalacetic transaminase) (Data are presented as mean ± SD, $n = 3$ mice, one-way ANOVA multiple comparison test, the absence of a P-value signifies no statistical significant difference between the groups ($P > 0.05$)). **E** TUNEL staining on the treated eyes in the MCNs/Ln/GD/FR(IV) and MCNs/Ln/GD/FR(IVT) groups (R: Retina, T: Tumor, $n = 3$ mice).

https://doi.org/10.1038/s41467-025-60454-5

the tail vein, resulting in lower presence at other sites and minimal impact on non-tumor areas.

Possible antitumor mechanism of MCNs/Ln/GD/FR NPs

To investigate the underlying mechanism by which MCNs/Ln/GD/FR NPs inhibit melanoma tumor growth, single-cell RNA sequencing technology was employed to analyze the compositional changes in melanoma tumor cells derived from mice in both the MCNs/Ln/GD/FR and PBS groups. Although these data may not fully reflect the characteristics of primary tumors, they are of substantial significance in elucidating the action mechanism of MCNs/Ln/GD/FR in suppressing tumor growth. Moreover, this investigation provides invaluable directional insights and data support for the potential application of these materials in the treatment of various types of tumors. Specifically, this study collected 9650 cells for the PBS group and 7361 cells for the MCNs/Ln/GD/FR group (indicated as "T" in the figures). Based on principal component analysis of gene expression profiles, 8 clusters of cells with specific gene expression profiles were identified, including *CSRNP1*$^+$ tumor, *PHLDA1*$^+$ tumor, *ANK3*$^+$ tumor, *BIRC5*$^+$ tumor, *ZNF90*$^+$ tumor, *TEX14*$^+$ tumor, and *OASL*$^+$ tumor (Fig. 7A–C). Significant differences were observed in the expression of heat shock protein (HSP)-related coding genes under the intervention of photothermal treatment, suggesting that photothermal ablation activated HSP-related signaling pathways (Fig. 7D). The significant downregulation of HSP-associated proteins in both general tumors and *ZNF90*$^+$ tumors in the treatment groups indicates that the GA released by MCNs/Ln/GD/FR

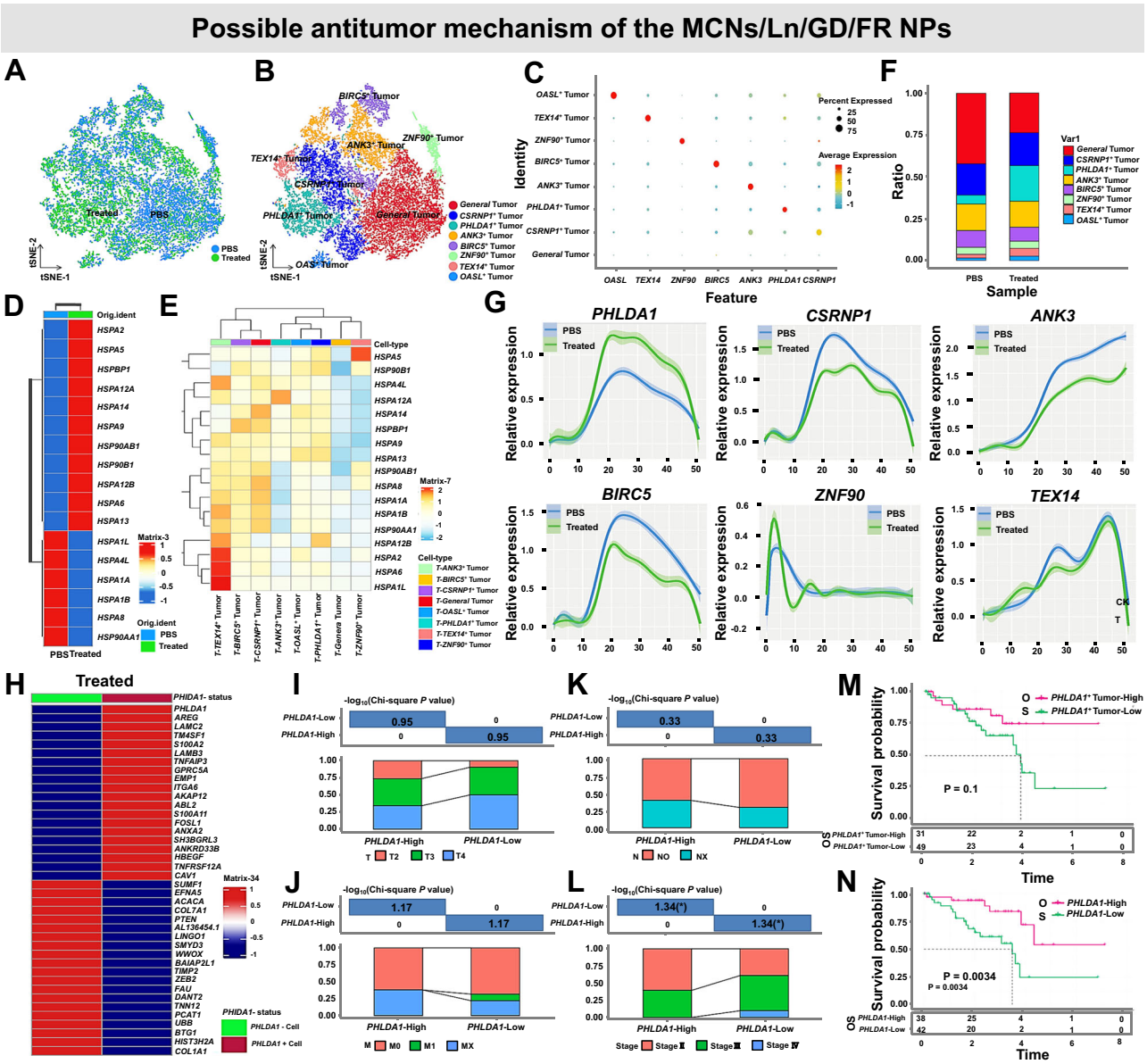

Fig. 7 | Single-cell RNA sequencing analysis of PBS and MCNs/Ln/GD/FR groups in melanoma. **A**–**C** 8 clusters with specific gene expression profiles were obtained from two treatment groups. **D** The expression of heat shock protein (HSP)-related coding genes. **E** The variation of HSP-associated proteins in different clusters in the MCNs/Ln/GD/FR groups. **F** The percentage of different clusters in the two treatment groups. **G** Survival differences between *PHLDA1*-positive cell High/Low enrichment groups and *PHLDA1* gene High/Low expression groups analyzed by two-sided log-rank tests (no multiple comparison adjustment applied, as these were pre-specified independent hypotheses). **H** Top 20 differential expression genes between *PHLDA1* + and *PHLDA1*- tumor cells in MCNs/Ln/GD/FR group. **I**–**L** Associations between *PHLDA1* expression groups and clinical stages. **I** T-stage distribution. **J** N-stage distribution. **K** M-stage distribution. **L** Stage distribution (Two-sided Chi-square tests with Benjamini-Hochberg adjustment). **M**, **N** Kaplan-Meier survival analysis for different *PHLDA1* groups.

NPs can downregulate HSPs expression, prevent damaged cancer cells from being repaired, and weaken thermal resistance caused by photothermal therapy (Fig. 7E).

To elucidate the influence of MCNs/Ln/GD/FR NPs on tumor cytotoxicity, Pseudobulk analysis was performed to identify differentially expressed genes. *SERPINE2*, *AKAP12*, *SLC16A13*, and *CXCL8* gene showed a significant increase in expression under MCNs/Ln/GD/FR NPs intervention, whereas *ARC*, *NR4A3*, and *RIMKLB* gene expression were upregulated in the PBS group (Supplementary Fig. 36A). Apoptosis inhibitory factor containing caspase recruitment domain (ARC) is an effective inhibitor of cell apoptosis that is induced and confers chemoradioresistance in human breast cancer[35,36]. AKAP12 (a-kinase anchoring protein 12), which acts as a regulator of mitosis by anchoring key signaling proteins such as PKA, PKC, and cyclins, is a protein kinase C substrate and potential tumor suppressor[37]. It can be downregulated by several oncogenes and strongly suppressed in various cancers. The enhancement of AKAP12 levels in the MCNs/Ln/GD/FR group facilitates the prognosis of tumor-bearing mice. Besides, the area under the curve (AUC) method with normalized gene set data from MSigDB's 'Hallmark Pathways' was further used to analyze the results[38]. The normalized enrichment scores (NES) of each pathway were plotted. Under MCNs/Ln/GD/FR NPs intervention, numerous signaling pathways that inhibit tumor cell proliferation, differentiation, and metastasis were activated, such as TNFa signaling via NFKB, G2M checkpoint, and MYC targets V1, besides significant changes in the tumor metabolic microenvironment (Supplementary Fig. 37 and Supplementary Fig. S38). These changes facilitate the inhibition of metabolic pathways favorable for tumor proliferation and metastasis.

Meanwhile, a distinct cells subgroup, labeled as *PHLDA1*$^+$ tumor cells, can be observed under the intervention of MCNs/Ln/GD/FR NPs (Supplementary Fig. 36B, C). This subgroup accounted for 21.3% of the total population in the MCNs/Ln/GD/FR group, while only 5.3% in the PBS group (Fig. 7F). Among the different gene expression patterns of the marker genes in the pseudo-time trajectory, the expression level and duration of *PHLDA1* gene increased obviously, indicating that the intervention of MCNs/Ln/GD/FR NPs can facilitate high-expression of *PHLDA1* gene in tumor cells (Fig. 7G). Downregulation of *PHLDA1* can promote cancer cell proliferation and migration, resulting in poor prognosis[35]. *PHLDA1*$^+$ and *PHLDA1*$^-$ tumor cells were further compared with only the top 20 upregulated and downregulated genes across the entire dataset considered. Different from *PHLDA*$^-$tumors, the upregulated and downregulated gene profiles in *PHLDA1*$^+$ tumor cells were inconsistencies for the MCNs/Ln/GD/FR group (Fig. 7H). It is reported that PHLDA1 may mediate drug resistance in receptor tyrosine kinase-driven cancers. Its level can be downregulated when breast cancer or renal cancer patients receive RTK-targeted therapy or HER2$^+$ breast cancer cells receive trastuzumab treatment, resulting in an increased resistance to drugs[34]. Exposed to MCNs/Ln/GD/FR NPs environments, the IC50 values for various anti-tumor drugs decrease obviously in *PHLDA1*$^+$ tumor cells relative to *PHLDA*$^-$ ones, indicating enhanced anti-tumor efficacy (Supplementary Fig. 39). Thus, MCNs/Ln/GD/FR NPs may enhance their anti-tumor effects by upregulating PHLDA1 level in tumor cells, leading to the differentiation of tumor cells towards sensitivity to DOX. Besides, pseudobulk analysis on *PHLDA1*$^+$ tumor cells was also carried out. The protein-protein interaction (PPI) network of up-regulated differentially expressed genes (DEGs) revealed that BMP2 and SNAI2 exhibited strong interactions with numerous other up-regulated proteins (Supplementary Fig. 40A). Conversely, the PPI network of down-regulated DEGs demonstrated interactions among EGR2, EGR3, DUSP2, NR4A1, NR4A2, and BTG2 (Supplementary Fig. 40B). Enrichment analysis of Gene Ontology (GO) and Kyoto Encyclopedia of Genes and Genomes (KEGG) revealed that the tumor cells exhibited enhanced oxidative stress response and activation of tumor necrosis factor superfamily pathways under the intervention of MCNs/Ln/GD/FR NPs, such as "response to oxidative stress" and "positive regulation of tumor necrosis factor production" (Supplementary Fig. 40C, D). These findings suggest that the cytotoxic effect of MCNs/Ln/GD/FR NPs on tumors can be enhanced by upregulating cell cycle-related protein expression to inhibit tumor mitosis and downregulating apoptosis-related proteins to promote tumor cell apoptosis.

The impact of *PHLDA1*$^+$ cell levels on overall survival rate was also analyzed using CIBERSORT, and the features of the *PHLDA1*$^+$ tumor group identified by scRNA to TCGA-UVM were mapped in both binary and continuous models. According to the expression level of PHLDA1 in TCGA-UVM, high and low expression groups were divided. The results indicated that the prognosis of high *PHLDA1* expression groups was better, they had fewer cases of T4 staging and M1 metastasis, as well as lower stage classification (Fig. 7I–L), indicating that higher levels of *PHLDA1*$^+$ are favorable to the overall survival rates (Fig. 7M, N).

Thus, the developed MCNs/Ln/GD/FR NPs was suggested to have a significant cytotoxic effect on melanoma. It can activate tumor-suppressive signaling pathways while inhibit proliferation and differentiation-related signaling pathways, ultimately induce tumor cell differentiation and increase sensitivity to DOX, result in an enhanced therapy effect.

In this study, double stimuli-responsive carbon-based lanthanide oxysulfide up-conversion nanocomposites with obvious photothermal conversion efficiency were developed to treat ocular in situ and subcutaneous melanoma-1. The introduction of a coating of lanthanide oxysulfide up-conversion material ($Y_2O_2S:Yb^{3+},Er^{3+}$) on MCNs can enhance its photothermal conversion efficiency from an initial 59.48% to 82.86% under 980 nm laser irradiation. The temperatures can rise dramatically to 50 °C within 150 s under the influence of a 280 mW cm^{-2} 980 nm laser, a level sufficient to eradicate cancer cells. While the loading of GA, DOX, as well as the linkage of FA and R8, can further enhance the photothermal synergistic therapy effect, and the coating of double stimuli-responsive hydrogel (PNIPAM) can ensure controlled drug release and safe delivery to tumors. Cell and animal evaluation results indicate that the developed MCNs/Ln/GD/FR NPs had a strong photothermal synergistic therapeutic efficacy, which can greatly reduce OCM-1 cell activity and melanoma growth. Single-cell RNA sequencing results revealed that MCNs/Ln/GD/FR NPs can enhance the therapy effect by activating tumor-suppressive signaling pathways while inhibiting proliferation and differentiation-related signaling pathways, ultimately induce tumor cell differentiation and increasing sensitivity to DOX. Insights gained from this research may prove to be vital to the development of cutting-edge therapeutic applications of optical therapy in the future.

Methods

Ethics Statement

Female Balb/c nude mice (3–4 weeks old, 20 g) were acquired from the SLRC Laboratory (Shanghai, China) following approval and in compliance with Ethical Committee of EYE and ENT Hospital of Fudan University (IACUC-DWZX-2021-013), in strict accordance with the ARVO Statement for the Use of Animals in Ophthalmic and Vision Research. All experimental protocols adhered to the IACUC Guideline, which mandated a maximum permissible tumor volume of 2000 mm^3 for mice. Tumor dimensions did not exceed 2 cm in any axis throughout the experiments. Tumor progression and animal welfare were monitored every 2–3 days, with documentation confirming adherence to ethical and volumetric constraints throughout the study.

Materials and reagents

Phenol, formalin, NaOH, Pluronic F127 (*Mw* = 12600, PEO106PPO70-PEO106), lanthanide oxides (Yb_2O_3, Y_2O_3, and Er_2O_3), sulfur, urea, gambogic acid (GA), doxorubicin (DOX), sodium dodecyl sulfate (SDS), N, N′-bis(acryloyl) cystamine (BAC), N-Isopropylacrylamide (NIPAM), potassium persulfate (KPS), N-hydroxysuccinimide (NHS),

and 1-ethyl-3-(3-(dimethylamino)propyl) carbodiimide (EDC), folic acid (FA), and glutathione (GSH) were purchased from Aladdin Industrial Inc. The R8 peptide was obtained from QYAOBIO (ChinaPeptides Co., Ltd.). Gibco supplied Fetal Bovine Serum, Trypsin-EDTA (1), and Fetal Bovine Serum. Sigma-Aldrich supplied DMEM-high glucose and Dimethyl sulfoxide. Shanghai Biyuntian Biotechnology Co., Ltd supplied Hoechst 33342, while Tongren Chemical Technology Co., Ltd supplied Cell Counting Kit-8(CCK-8), Calcein-AM, and PI. All reagents were used just as they were obtained, without further purification.

Lanthanide nitrates ($Y(NO_3)_3$, $Yb(NO_3)_3$, and $Er(NO_3)_3$) were synthesized by dissolving Yb_2O_3, Y_2O_3, and Er_2O_3, respectively, in dilute HNO_3 under agitation with heating (keep boiling), and then evaporating the water to yield the desired product.

Synthesis of various nanocomposites

Synthesis of MCNs nanoparticles. Ordered MCNs precursor can be prepared using a two-step method as reported previously[39]. In a typical synthesis, 0.6 g of phenol and 2.1 ml of formalin aqueous solution (37 wt %) were initially added to 15 ml of NaOH aqueous solution (0.1 M) under stirring at 70 °C for 0.5 h. The mixture was then heated to 66 °C, and 15 ml of triblock copolymer Pluronic F127 aqueous solution (0.96 g F127) was added while stirring. After 2 h of reaction, 50 ml of water was slowly added under stirring. The color of the reaction solution changed from colorless to pink and then to scarlet. The reaction was stopped after 18 h of stirring at 66 °C, and the reaction mixture was allowed to stand until the deposit dissolved. Subsequently, 17.8 mL of the crimson solution was added to 56 mL of deionized water under stirring for 30 min before being transferred to a 100 mL autoclave, which was maintained at 130 °C for 24 h. The resulting MCNs precursor was then centrifuged, washed three times with distilled water, and dried at room temperature. The final MCNs nanoparticles were obtained by heating at 700 °C for 2 h under an N_2 atmospheres at a heating rate of 2 °C min^{-1}.

Synthesis of MCNs/Ln NPs. The monodisperse MCNs/Ln precursor was synthesized according to our previous report with minor modification[40]. In a typical synthesis of the MCNs/Ln precursor, varying stoichiometric ratios (5%, 10%, 15%Yb; 2%Er) and amounts (0.5, 0.75, 1 mmol) of lanthanide nitrate were added into 30 mL of MCNs precursor aqueous solution (0.125 g) with the assistance of ultrasonication for 15 min. Then, 3.0 g of urea was dissolved in the solution by stirring. The mixture was then transferred to a round-bottom flask and heated at 85 °C for 3 h with stirring. The precursor was collected by centrifugation, washed three times with deionized water and ethanol, and dried at 60 °C in air. The final MCNs/Ln NPs were obtained by heating them at different temperatures for 2 h in an N_2/S atmosphere at a heating rate of 2 °C min^{-1}.

Photothermal Performance of the Synthesized Nanocomposites. The photothermal performance of the synthesized nanocomposites was performed as follows: After exposure to a 980 nm laser (3 W, Beijing Laserwave OptoElectronics Tech. Co., Ltd.) with different power densities (Power density (mW cm^{-2}) = Laser power (mW)/Laser beam area (cm^2)), the temperature changes of the obtained nanocomposite aqueous dispersion with different concentrations were monitored by a JK808 Multichannel temperature tester and a FOTRIC 220 series hand-held thermal imager.

The photothermal conversion efficiency (η) of Y_2O_2S:Yb^{3+},Er^{3+}, MCNs and MCNs/Ln NPs (0.75 mmol) was calculated according to the photothermal conversion equations:

$$\eta = (hA\Delta T_{max} - H_s)/[P(1 - 10^{-Abs})]$$

where ΔT_{max} is the maximum change in temperature, H_s is the heat relating to the absorption value of water, Abs is the absorption value of the three kinds of materials at 980 nm, and P is the laser power.hA was determined using another equation:

$$hA = mC_p/\tau,$$

where τ is the slope of the linear data from the cooling time vs −ln(θ) (Supplementary Fig. 13) and C_p and m are the water heat capacity and the mass, respectively. It was also needed to introduce θ ($\Delta T/\Delta T_{max}$).

Synthesis of MCNs/Ln/G NPs. Taking advantage of the large specific surface area and physical adsorption capacity of MCNs, gambogic acid (GA) was loaded into the MCNs/Ln NPs. 20 mg of MCNs/Ln NPs and 5 mg of GA were initially added to a brown glass bottle. Then, 4 mL of anhydrous ethanol was added with the assistance of ultrasonication for 20 min, and the obtained mixture was further stirred in the dark for 24 h. After centrifugation at 10000 rpm for 10 min, MCNs/Ln/G NPs were collected. Meanwhile, the content of GA in the supernatant solution was measured using a UV−vis Spectrophotometer.

The measurements of GA release from MCNs/Ln/G NPs were performed by dispersing the obtained MCNs/Ln/G NPs in 1 mL of PBS solution and transferred them into a dialysis tube, which was then placed into a 15 mL centrifuge tube containing 10 mL of PBS under gentle shaking at 37 °C. Subsequently, 1 mL of supernatant was collected, and another 1 mL of fresh PBS solution was added at certain time intervals (0, 0.25, 0.5, 1, 2, 4, 6, 8, 12, 24, 36 and 48 h). The amount of GA was further calculated by comparing it with the standard curve of the GA aqueous solution.

Synthesis of MCNs/Ln/G/pNIPAM NPs. Firstly, 0.144 g of sodium dodecyl sulfate (SDS) was added into 50 mL of deionized water in a three-neck flask and stirred in an argon atmosphere for 30 min. Then, 0.5658 g of N-Isopropylacrylamide (NIPAM) dispersed in 5 mL of deionized water and 5 mL of N, N′-bis(acryloyl) cystamine (BAC) (0.052 g) ethanol solution were added to the above solution, which was further stirred for 1 h until a transparent solution was obtained. Subsequently, 5 mL of the MCNs/Ln/G aqueous mixture was added to the solution under vacuum and stirred for another 1 h in an argon atmosphere. When 1 mL of potassium persulfate (KPS) (0.0135 g) solution was added, the obtained mixture was heated to 60 °C for 1 h. After the reaction, the flask was immediately cooled in an ice bath, and the precipitate was separated by centrifugation at 10000 rpm for 10 min. The obtained MCNs/Ln/G/pNIPAM NPs were dispersed in deionized water and then preserved at 4 °C.

Synthesis of MCNs/Ln/GD NPs. Utilizing the mesh-like properties of the pNIPAM layer to further adsorb and load doxorubicin (DOX). The obtained MCNs/Ln/G/pNIPAM NPs were initially dispersed in 2 mL of deionized water in a brown glass container. Next, 10 mg of DOX was added and dissolved in the mixture. After 24 h of steady stirring, the precipitate was separated by centrifugation at 10000 rpm for 10 min, and the supernatant was retained. The concentration of DOX in the supernatant solution was determined using a UV−vis Spectrophotometer.

Due to the temperature and GSH stimuli-responsive properties of PNIPAM hydrogels where DOX was encapsulated, the release rate kinetics of DOX were measured under heating or GSH environments. For the release of DOX from MCNs/Ln/D NPs in a GSH environment, similar to the measurements of GA release from MCNs/Ln/G NPs, deionized water, 0.5 mM and 1 mM GSH solution were used to substitute PBS. While for the release of DOX from MCNs/Ln/D nanocomposites under heating, 56 °C warm water was used to imitate the irradiation of a 980 nm laser, with other conditions similar to the measurement of GA release from MCNs/Ln/G NPs. The 1.5 mL centrifuge tube was gentle shaken in 56 °C warm water, with time intervals controlled at 1, 2, 3, 4, 5, 6, 7, 8, 9, 10 min.

Meanwhile, the DOX release performance under the irradiation of a 980 nm laser was investigated. The MCNs/Ln/GD NPs were dispersed in 1 mL of PBS solution before being placed onto two slides and covered with a cover glass. One slide was exposed to a 280 mW cm^{-2} 980 nm laser for 10 min, while the other slide, serving as the control group, was left untreated. Then, fluorescence microscope images of the two samples were collected.

Synthesis of MCNs/Ln/GD/FR NPs. 20 mg of folic acid (FA), 10 mg of 1-ethyl-3-(3-(dimethylamino) propyl) carbodiimide (EDC), and 10 mg of N-hydroxysuccinimide (NHS) were added to a 10 mL PBS buffer solution and stirred for 4 h. Then, the MCNs/Ln/GD NPs were added, and the resulting mixture was stirred for another 12 h. The precipitate, which was separated by centrifugation at 10000 rpm for 10 min, was further dispersed in 10 mL of PBS, and 1 mg of R8 peptide was added. Following another 12 h of stirring, the final MCNs/Ln/GD/FR NPs were obtained after being separated by centrifugation at 10000 rpm for 10 min.

In vitro cell evaluation of nanocomposites

The Global Bioresource Center provided the human retinal microvascular endothelial cells (hRMEC), human retinal epithelial cells (ARPE-19), human embryonic kidney epithelial cells (HEK 293 T), mouse fibroblast cells L929, and OCM-1 cell lines (a M14 derivative) were provided by the BeNa Culture Collection. All cell lines have been authenticated by the STR method and routinely screened for mycoplasma routinely.

Cytotoxicity evaluation. In vitro cytotoxicity assays were conducted as follows: 5×10^3/well ARPE-19 cells were seeded into 96-well plate and incubated at 37 °C for 24 h for cell adherence. Different materials, including MCNs, MCNs/Ln, MCNs/Ln/G, MCNs/Ln/GD, and MCNs/Ln/GD/FR, were added to the corresponding wells at various concentrations. For each group, more than six samples were prepared and measured. The cell incubation time was set to 24 h.

Cell viability was measured using the Cell Counting Kit-8 (CCK-8, CK-04, Dojindo), and the experiment was repeated three times.

The same procedure was s applied to hREMC, 293 T, and L929 cells as that used for ARPE-19 cells.

The relative cell viability was determined using the following equation:

$$\text{Cell viability}(\%) = (OD_{570,\text{sample}} - OD_{570,\text{blank}})/(OD_{570,\text{control}} - OD_{570,\text{blank}}) \times 100\%$$

Photothermal effects on OCM-1 cells. Before assessing the photothermal therapeutic impact of the synthesized nanocomposites on OCM-1 cells, the photothermal effect of a 980 nm laser on the cell was first evaluated to eliminate the laser's inherent photothermal effect. 5×10^3/well cells were seeded into 96-well plate and cultured at 37 °C for 24 h for cell adherence. Then, a 980 nm laser with different power densities was used to irradiate the cells for 10 min from a distance of 3 cm (the distance from the optical fiber head to the middle of the medium). After another 24 h incubation, the cellular survival rate after irradiation was detected using CCK-8, and the experiment was repeated three times.

Based on the above photothermal effect of the pure 980 nm laser on OCM-1 cells, a laser power density of 280 mW cm^2 was selected for subsequent experiments.

Meanwhile, a comprehensive evaluation of the photothermal effect induced by a 280 mW cm^{-2} laser on ARPE-19 cells was conducted. Initially, 5×10^3/well cells were seeded into 96-well plate and cultured at 37 °C for 24 h to ensure cell adherence. Then, a 980 nm laser with a power density of 280 mW cm^{-2} was employed to irradiate the cells for 10 min from a fixed distance of 3 cm. After another 24 h incubation, the survival rate of the irradiated ARPE-19 cells was assayed using CCK-8, and this procedure was replicated three times.

Furthermore, the photothermal effects of various nanocomposites (MCNs, MCNs/Ln, MCNs/Ln/G, MCNs/Ln/GD, MCNs/Ln/GD/FR) on OCM-1 cells were further evaluated using a similar methodology. After cell adherence, the medium was substituted with fresh medium containing the nanocomposites at concentrations of 50, 100, and 200 μg mL^{-1}. After an additional 6-hour incubation, the cells were irradiated with a 980 nm laser at 280 mW cm^{-2} for 10 min from a distance of 3 cm. Subsequently, after a 24 h incubation, the cellular survival rate was determined using CCK-8, and this process was repeated three times for each nanocomposite.

Calcein-AM/PI double staining. To study the photothermal therapeutic effect of different nanocomposites on OCM-1 cells under the irradiation of a 980 nm laser, Calcein-AM/PI double staining was employed to ascertain the number of live and dead cells. Green fluorescence can be detected in living cells, while red fluorescence is observed in dead cells under a fluorescence microscope. After being co-cultured with various nanocomposites (MCNs, MCNs/Ln, MCNs/Ln/G, MCNs/Ln/GD, MCNs/Ln/GD/FR) at a concentration of 200 μg mL^{-1} for 24 h, the cells were washed with PBS and replaced with fresh culture medium. Then, the cells were irradiated with a 980 nm laser at 280 mW cm^{-2} for 10 min from a distance of 3 cm. Following irradiation, the cells were co-cultured for an additional 24 h. A group that received no treatment (neither nanocomposites nor laser irradiation) served as the control group, termed "Medium". Calcein-AM/PI solution was added and incubated for 15 min, and the distribution of living and dead cells was observed and photographed using a DMI8 inverted fluorescence microscope ($n = 3$).

Cell apoptosis assessment. OCM-1 cells were planted in 96-well plates and incubated for 24 h at 37 °C. After that, the medium was replaced with new media containing MCNs, MCNs/Ln, MCNs/Ln/G, MCNs/Ln/GD, and MCNs/Ln/GD/FR (200 μg mL^{-1}). After 24 h incubation, the cells were washed with PBS and replaced with fresh culture medium. The cells were then exposed to a 980 nm laser (280 mW cm^{-2}, 10 min). A group that received laser irradiation treatment served as the control group, termed "Medium + Laser"). After another 24-h incubation, cells were collected by trypsin digestion, washed with PBS, and resuspended in 300 μL 1X binding buffer. Then, 4 μL Annexin V-FITC and 1.5 μL PI were added in sequence. After being kept in the dark for another 15 min, all samples were analyzed using an Accuri C6 flow cytometer to evaluate cell viability.

Western blotting analysis. The OCM-1 cells were harvested and lysed on ice using RIPA Lysis Buffer (Beyotime, Shanghai, China). Protein concentration was determined using a BCA Protein Assay kit (Beyotime). Subsequently, 40 μg of protein samples were loaded onto each lane and separated using 10% SDS-PAGE. The proteins were then transferred to polyvinylidene fluoride (PVDF) membranes. To reduce non-specific binding, the membranes were blocked with 5% skimmed milk for 2 h at room temperature. After blocking, the membranes were incubated overnight at 4 °C with primary antibody at the following concentrations: HSP 70 (1:2000, ABclonal) and HSP 90 (1:2000, Proteintech) diluted in Tris-buffered saline with Tween 20 (TBST). Then, the membranes were incubated with an HRP-conjugated secondary antibody (1:10000, Jackson Immunoresearch, Tucker, GA) for 1.5 h at room temperature. The blots were visualized using an enhanced chemiluminescence (ECL) reagent, and their expression levels were quantified using ImageJ software (Version 1.8.0, Bethesda, MD, USA).

The knockdown of HSP 70 protein on photothermal inhibitory effects of OCM-1. Initially, 2×10^5 OCM-1 cells were seeded into a 6-well plate and cultured overnight. The siRNA was encapsulated in

lipid nanoparticles as previously reported[41]. The cells were transfected with either siRNA1^{HSPA1A} or siRNA2^{HSPA1A} to knock down the expression of HSP70, and their sequences were listed in Supplementary Table 1. Following a 48-h incubation, the cells were lysed to facilitate the extraction of proteins for subsequent western blot analysis. Briefly, the proteins were separated and transferred onto polyvinylidene difluoride membrane, followed by incubation with HSP70 antibody (1:2000, A23457, Abclonal) and β-actin (1:5000, AC004, Abclonal) overnight. The membranes were then stained with IRDye® secondary antibodies (1:20000, Licor, USA) and visualized using an Odyssey® DLx Imaging System (Licor, USA).

Subsequently, thermal damage models were established to evaluate the impact of HSP70 on cellular heat-resisting property. A total of 8×10^3 cells were seeded into a 96-well plate and cultured overnight. Following a 48 h transfection with siRNA2^{HSPA1}, the cells were subjected to two distinct thermal damage models. In the first model, cells were exposed to medium with or without 100 μg mL^{-1} MCNs/Ln-NPs for 6 h. Subsequently, they were irradiated with a 980 nm laser at a power density of 280 mW cm^{-2} for 10 min, with the optical fiber head positioned 3 cm away from the center of the culture medium. In the second model, the cells were subject to a heat shock treatment at 45 °C in an incubator for 15 mins. Cell viability was evaluated 24 h post-thermal damage utilizing the CCK-8 method.

In vivo anticancer evaluation of nanocomposites

To assess the synergistic therapeutic efficacy of MCNs/Ln/GD/FR nanocomposites in tumor treatment, two kinds of melanoma models were established: subcutaneous tumors and in situ ocular tumors.

During the model induction and treatment periods, the mice were housed in individually ventilated cages (IVC). The environmental conditions within the housing facility were maintained with the temperature controlled within the range of 21–23 °C and the relative humidity kept at a range of 40–60%. A standard photoperiod of 12 h of light followed by 12 h of darkness was regulated. Throughout the entire experimental period, the animals were provided with unrestricted access to food and water.

Anticancer evaluation in subcutaneous melanoma model. Subcutaneous OCM-1 melanoma tumors were induced by injecting 2×10^7 OCM-1 cells suspended in 0.1 ml serum-free RMPI-1640 media into the back region of each mouse. Upon reaching a tumor volume of 200–400 mm^3, mice with comparable tumor sizes were randomly divided into 5 groups ($n = 5$ per group): PBS, Laser, DOX, MCNs/Ln/GD, and MCNs/Ln/GD/FR. Subsequently, 200 μL PBS, DOX (10 μM), MCNs/Ln/GD (2 mg kg^{-1}), or MCNs/Ln/GD/FR (2 mg kg^{-1}) were administered via caudal vein injection. Tumors in the Laser, MCNs/Ln/GD, and MCNs/Ln/GD/FR groups were irradiated with a 280 mW cm^{-2} 980 nm laser for 10 min at a 3 cm distance, 4 h post-injection. Thermal imaging documented tumor site temperatures at regular intervals. Tumor volumes and body weights were measured every 2–3 days. The tumor volumes were measured using a caliper, and estimated using the following equation:

$$Vt = 0.5 \times a \times b \times b$$

(where a and b represent the macro and minor axis of tumor). Relative tumor volumes were determined by:

$$\Delta V = (V_t - V_0)/V_0 \times 100\%$$

(V_0 is the initial tumor volume at treatment onset).

On day 21, mice were sacrificed, and organs (heart, liver, spleen, lung, kidney) and tumors were collected. Thermal imaging and histopathological examinations were conducted on these tissues.

Anticancer evaluation in in situ melanoma model. Under systemic anesthesia, topical proparacaine (Alcon, USA), and tropicamide phenylephrine (Santen Pharmaceutical, Japan), an in situ melanoma model was established by a skilled ophthalmologist under a surgical microscope. A small tunnel was created 1 mm posterior to the limbus using an insulin syringe (BD, USA). Subsequently, a total of 4×10^4 OCM-1-Luc cells (2 μL volume) were injected subretinally into the left eyes of nude mice using a Hamilton injector equipped with a 33 G flat head needle and a 10 μL syringe. Tumor growth was monitored via bioluminescence imaging on days 7 and 14 post-injection, utilizing an in vivo optical imaging system (PerKinElmer, Spectrum CT) after intraperitoneal administration of 200 μL 15 mg mL^{-1} D-Luciferin Sodium Salt (Solarbio). On days 8 and 15 after injection of OCM-1-Luc cells, 100 μL PBS (IV), 100 μL DOX (10 μM, IV), 100 μL MCNs/Ln/GD (2 mg mL^{-1}, IV), 100 μL MCNs/Ln/GD/FR (2 mg mL^{-1}, IV) and 100 μL MCNs/Ln/GD/FR (2 mg mL^{-1}, IVT) were injected into mice through tail intravenous injection (IV) or intravitreal injection (IVT). 4 h post-IV injection, tumors were irradiated with a 280 mW cm^{-2} 980 nm laser for 7 min, with temperature variations of the eye recorded using an infrared thermal imager (Hikmicro, DS-2TP74-H25PCKJ/W). The same procedure was executed for the MCNs/Ln/GD/FR (IVT) group after 24 h injection. On day 21, eyeballs were collected, weighed, and processed for paraffin histopathological analysis.

Quantitative Analyses of Y Concentration using ICP. Tumor tissues of the mice in different groups and the major organs (heart, liver, spleen, lung, kidney) for the mice treated with MCNs/Ln/GD/FR NPs were collected, homogenized, lyophilized, and analyzed for Y^{3+} uptake content by ICP analysis to assess biodistribution.

Histopathological analysis. Following a 10% formalin fixation, the tumor or organs were dehydrated in graded ethanol, embedded in paraffin, and sectioned into 4–5 μm. Following a series of dehydration sections and other preparations, hematoxylin was applied dropwise to fill the section for 10 min before being rinsed with PBS. Then, eosin was used for staining the extracellular matrix for 8 min. The samples were then examined under a light microscope (Leica DM750).

Hemolysis Assay. To evaluate the hemocompatibility of MCNs/Ln/GD/FR NPs, rabbit blood was collected and centrifugated at $2000 \times g$ min^{-1} for 10 min at 4 °C to isolate the red blood cells, which further washed and diluted with PBS solution by 10 times. Then, 0.1 mL of the diluted red blood cells were added to 0.4 mL of PBS solution (negative control group), deionized water (positive control group), and MCNs/Ln/GD/FR NPs dispersion with different concentrations (sample group). The samples were incubated at 37 °C for 4 h, after which they were centrifuged at $300 \times g$min^{-1} for 10 min at 4 °C. Finally, the absorbance of the supernatant was measured using an Agilent Synergy H1 microplate reader ($n = 5$ per group).

The hemolysis percentage was calculated using the following formula:

$$\text{Hemolysis}(\%) = (A_{\text{sample}} - A_{\text{negative control}})/(A_{\text{positive control}} - A_{\text{negative control}}).$$

Biochemistry tests. Blood samples collected days 15 and 30 were centrifuged at 3000 rpm for 15 min to obtain serum, which was analyzed using a Mindray BC-2800vet system to assess liver and kidney biochemistry function, providing insights into systemic physiological responses ($n = 4$ per group).

TUNEL staining and HSP fluorescent staining. The terminal deoxynucleotidyl transferase-mediated dUTP nick-end labeling (TUNEL) apoptosis assay was conducted to identify apoptotic cells within the tumor and adjacent normal tissues, utilizing a One-step TUNEL FITC Apoptosis Detection Kit (APExBIO, USA), following the

manufacturer's instructions ($n = 3$ per group). Meanwhile, an assessment of HSP was conducted in both untreated and treated tumors. Specifically, the expression levels of HSP 70 (1:200, ABclonal) and HSP 90 (1:200, Proteintech) were assessed through fluorescent staining and visualized using a fluorescent microscope (APX 100, Olympus) ($n = 3$ per group).

Single-cell RNA-seq data processing

Sample collection. Initially, mice bearing subcutaneous tumors were administered 100 μL of MCNs/Ln/GD/FR (2 mg mL^{-1}) via caudal vein injection. 6 h post-injection, the mice were subjected a 980 nm laser irradiation for 10 min at a power density of 280 mW cm^{-2}, with the laser positioned 3 cm from the tumor (measured from the optical fiber head to the tumor). After 24 h of photothermal therapy, tumor tissues were carefully collected and stored in a specialized solution. an untreated group served as the control for comparative analysis. Subsequent sample processing and data collection were conducted by CapitalBio Technology.

Single-cell RNA sequencing. Employing the single-cell 3' Library and Gel Bead Kit V3.1 (10x Genomics, 1000121) along with the Chromium Single Cell G Chip Kit (10x Genomics, 1000120), we processed a cell suspension containing 300–600 live cells per microliter, as verified by Count Star. This suspension was loaded onto the Chromium single-cell controller (10x Genomics) to generate single-cell gel beads in emulsion, following the manufacturer's protocol. Briefly, individual cells were suspended in PBS with 0.04% BSA, and approximately 6000 cells were introduced into each channel, aiming to recover around 3000 target cells.

Cell capture and cDNA synthesis. Using the same kits mentioned above, we processed a cell suspension containing 300–600 living cells per microliter, as determined by Count Star. The suspension was loaded onto the Chromium single-cell controller (10x Genomics) to generate single-cell gel beads in emulsion, adhering to the manufacturer's protocol. Single cells were suspended in PBS with 0.04% BSA, and roughly 6000 cells were introduced into each channel to recover approximately 3000 target cells. Captured cells were lysed to release RNA, which was subsequently barcoded through reverse transcription within distinct GEMs. Reverse transcription was performed using an S1000TM Touch Thermal Cycler (Bio Rad) with a temperature profile of 53 °C for 45 min, ramping up to 85 °C for 5 min, and maintained at 4 °C. Following this, cDNA was synthesized, amplified, and its quality was evaluated using an Agilent 4200 system (analysis conducted by CapitalBio Technology, Beijing).

Single cell RNA-Seq library preparation. Single-cell RNA-seq libraries were constructed using the Single Cell 3' Library and Gel Bead Kit V3.1, following the manufacturer's guidelines. These libraries were sequenced using an Illumina Novaseq6000 sequencer, achieving a sequencing depth of at least 100,000 reads per cell with a pair-end 150 bp (PE150) sequencing strategy. This was executed by CapitalBi Technology in Beijing.

Data preprocessing

Cellranger pipeline. The Cell Ranger software was downloaded from the 10x Genomics website (https://support.10xgenomics.Com/single-cell-gene-expression/software /down loads/latest). Using the cellranger count module, processes such as alignment, filtering, barcode counting, and UMI counting were carried out to produce a feature-barcode matrix and determine clusters. For dimensionality reduction, PCA (Principal Component Analysis) was applied, and the first ten principle components were utilized to generate clusters through both the K-means algorithm and a graph-based algorithm.

Seurat pipeline. An alternative clustering method employed was Seurat 3.0, an R package. Cells containing fewer than 200 genes, genes ranked in the top 1%, or mitochondrial gene ratio exceeding 25% were considered abnormal and filtered out. Dimensionality reduction was achieved using PCA, while visualization was facilitated by TSNE and UMAP.

Enrichment analysis. GO enrichment, KEGG enrichment, Reactome enrichment, and Disease enrichment (human only) of cluster markers were conducted using KOBAS software, employing the Benjamini-Hochberg multiple testing adjustment. The top 20 marker genes of each cluster were used for this analysis. The results were visualized using an R package.

PPI (protein-protein interaction). Protein-protein interaction data was retrieved from the STRING database, selecting interactions with a combine_score ≥ 400. For each cluster, the top 20 marker genes' interactions were specifically extracted from the database, and the interactions were visualized using Cytoscape software.

Transcription factor prediction. Using the TFBS Tools and JASPAR database, transcription factors were predicted within 2000 bp upstream and 500 bp downstream region of the transcription start site (TSS) for the top 20 marker genes in each cluster. Subsequently, the gene and transcription factor (TF) network for each cluster were visualized with Cytoscape software.

GSEA assay (Gene set enrichment analysis). GSEA was conducted using GSEA software version 2.2.2.4, relying on predefined gene sets sourced from the Molecular Signatures Database (MSigDB v6.2). All genes identified across all cells within a sample were utilized for the analysis. Gene expression data was derived by calculating the mean UMI count of genes within a specific cluster compared to the remaining cluster. The range for selecting gene sets from the collection was set between 0 and 500 genes.

Single-cell trajectories analysis. Single-cell trajectories were constructed using the Monocle (R package), which incorporates the concept of pseudotime. Genes were filtered based on the following criteria: they must be expressed in more than 10 cells, have an average expression value greater than 0.1, and exhibit a Q-value less than 0.01 across various analysis. In addition, Cell Cycle Phase (human and mouse only) was assigned using Seurat 3.0 with consistent parameters.

WGCNA. The weighted correlation network analysis (WGCNA) was conducted using the WGCNA R software package. Based on the aforementioned clustering result, each cluster was further segmented into sub-clusters, and the average gene expression within each sub-cluster was computed. The parameters utilized were the defaults provided by the software.

Cell type annotation. Cell type annotation was conducted using the singleR package (https://bioconductor.org/packages/devel/bioc/html/SingleR.html). This package performs unbiased cell type recognition from single-cell RNA sequencing data by referencing transcriptomic datasets of pure cell types to independently infer the cell of origin for each single cell. For human data, Blueprint_Encode or HPCA was utilized, while for mouse data, ImmGenor Mouse. RNAseq was employed.

Sequence alignment and data filtering. The "Cellranger" v7.1.0 count workflow with default settings was used to process the single-cell sequencing data for subsequent analysis, facilitating data quantification, genome alignment against the GRCh38 version (sourced from 10x Genomics), and preliminary data filtration. Then, the "DoubletFinder" v2.0.3 workflow was employed to process the filtrated data[42]. Data

from different groups underwent normalization separately. The canonical correlation analysis (CCA) algorithm was also applied to minimize batch discrepancies and unify the data sets. This harmonized dataset served as the foundation for more intricate analyses[43].

Cluster identification and annotation. Principal component analysis was conducted using the Seurat v4.3.0 package, and 9 distinct clusters with the "FindClusters" function were successfully identified. Subsequently, the "FindAllmarker" function was deployed to detect gene expression signatures for each cluster. These distinctively expressed genes were used for cluster annotations. Finally, the t-Distributed Stochastic Neighbor Embedding (tSNE) algorithm was used for data dimensionality reduction.

Differential expression and pathway enrichment analysis. Differential gene expression between PBS and MCNs/Ln/GD/FR groups can be discerned using "edgeR" workflow by adopting the pseudobulk strategy. Genes with an adj.p-value > 0.05 and |log2FC | > 0.5 were considered differentially expressed. These genes were then subjected to Gene Ontology (GO) and Kyoto Encyclopedia of Genes and Genomes (KEGG) pathway enrichment analyses for functional annotation[44]. Hallmark pathway gene sets from MSigDB and the "AUCell" v1.20.2 package were used to grade each cell based on the Hallmark pathways.

Trajectory inference and transcription factor activity analysis. By using the monocle v2.26.0 workflow, the differentiation trajectory of tumor cells was mapped out, inspecting gene expression trends over pseudotime. Transcription factor activity was evaluated using "pySCENIC", with the top 5 most active transcription factors visualized for each cluster[45].

Survival and drug sensitivity analysis. Through the "FindAllmarker" function, feature genes for each cluster (with criteria set at logFC > 0.8 & adj.*p*-value < 0.01) were identified. RNA-seq and pertinent clinical data for UVM from the TCGA database were retrieved. Based on the feature genes, CIBERSORT algorithm was employed to assess the cluster expression abundance for each TCGA-UVM patient[46]. The "survminer" v0.4.9 package was utilized to determine the optimal cutoff point, segmenting the TCGA-UVM data into high and low expression groups. The survival difference between the two groups was analyzed using the Kaplan-Meier survival analysis, and differences in clinical data between the groups were also evaluated. The "pRRophetic" v0.5.0 package was used to analyze the differential drug sensitivity between high and low expression groups, based on the Cancer Genome Project (CGP) 2016 data (Clinical drug response can be predicted using baseline gene expression levels and in vitro drug sensitivity in cell lines).

Other characterizations

A Smart lab 9 powder Diffractometer equipped with Cu K radiation ($\lambda = 1.54$ Å) was employed to analyze the phase structure and crystallographic properties of the synthesized nanocomposites. The morphology and microstructure of the samples were examined using a field emission scanning electron microscope (HITACHI S-7400, Japan) and a high-resolution transmission electron microscopy (JEM2100F, Japan) operated at an accelerating voltage of 200 kV. The surface functional groups of the nanocomposites were investigated via Fourier-transform infrared (FT-IR) spectroscopy, with spectra recorded in the range of 400 to 4000 cm^{-} using a Thermal Fisher Nicolet 6700 spectrometer (USA) and the KBr pellet technique. Brunauer-Emmett-Teller (BET) measurements were conducted on a surface area and porosimetry analyzer (QUANTACHROME, USA) to determine the specific surface area and pore size distribution of the materials. The emission spectra of the nanocomposites were recorded using a Hitachi F-7000 Fluorescence Spectrophotometer (Japan), while the UV−vis −NIR spectra were obtained with a Shimadzu UV-3600i Plus spectrophotometer (Japan). In addition, the Zeta potential of the samples was measured using Malvern ZETASIZER equipment (Nano-ZS90, Britain), providing insights into the surface charge and stability of the nanocomposites in dispersion.

Statistical analysis

All data are presented as the mean ± standard deviation (means ± SD). The significance between groups was determined using unpair *t* test, one-way analysis of variance (ANOVA), or two-way ANOVA in GraphPad Prism 8.0 software (ns: no significance; $^{*}P < 0.05$, $^{**}P < 0.01$, $^{***}P < 0.001$, $^{****}P < 0.0001$). Detailed information regarding sample sizes, comparison methods, and other relevant parameters is provided in the legends accompanying each figure.

Reporting summary

Further information on research design is available in the Nature Portfolio Reporting Summary linked to this article.

Data availability

The authors declare that all data supporting the findings of this study are accessible within the article and its Supplementary Information. Furthermore, the single-cell RNA sequencing data generated in this study have been deposited in the NCBI GEO database [https://www.ncbi.nlm.nih.gov/sra/PRJNA1236827] under accession number PRJNA1236827. Source data are provided in this paper.

References

1. Zhu, X. et al. Temperature-feedback upconversion nanocomposite for accurate photothermal therapy at facile temperature. *Nat. Commun.* **7**, 10437 (2016).
2. Zhang, R. et al. Structure engineered high piezo-photoelectronic performance for boosted Sono-Photodynamic therapy. *Adv. Mater.* **36**, 2308355 (2024).
3. Du, Y. et al. A vacancy-engineering ferroelectric nanomedicine for cuproptosis/apoptosis co-activated immunotherapy. *Adv. Mater.* **36**, e2403253 (2024).
4. Grillone, K. et al. An unbiased lncRNA dropout CRISPR-Cas9 screen reveals RP11-350G8.5 as a novel therapeutic target for multiple myeloma. *Blood* **144**, 1705–1721 (2024).
5. Bergeron, P. et al. Non-homogenous intratumor ionizing radiation doses synergize with PD1 and CXCR2 blockade. *Nat. Commun.* **15**, 8845 (2024).
6. Zhou, H. et al. Upconversion NIR-II fluorophores for mitochondria-targeted cancer imaging and photothermal therapy. *Nat. Commun.* **11**, 6183 (2020).
7. Du, Y. et al. Revealing the mutually enhanced mechanism of necroptosis and immunotherapy induced by defect engineering and piezoelectric effect. *Adv. Mater.* **36**, 2304322 (2024).
8. Li, X., Lovell, J. F., Yoon, J. & Chen, X. Clinical development and potential of photothermal and photodynamic therapies for cancer. *Nat. Rev. Clin. Oncol.* **17**, 657–674 (2020).
9. Liu, Y., Bhattarai, P., Dai, Z. & Chen, X. Photothermal therapy and photoacoustic imaging via nanotheranostics in fighting cancer. *Chem. Soc. Rev.* **48**, 2053–2108 (2019).
10. Tao, K. et al. Targeted multifunctional nanomaterials with MRI, chemotherapy and photothermal therapy for the diagnosis and treatment of bladder cancer. *Biomater. Sci.* **8**, 342–352 (2019).
11. Kim, M. et al. Micro-engineering and nano-engineering approaches to investigate tumour ecosystems. *Nat. Rev. Cancer* **23**, 581–599 (2023).
12. Chen, Z. et al. DNA Damage inducer mitoxantrone amplifies synergistic mild-photothermal chemotherapy for TNBC via decreasing heat shock protein 70 expression. *Adv. Sci.* **10**, e2206707 (2023).

13. Wang, F. et al. Black phosphorus/MnO2 nanocomposite disrupting bacterial thermotolerance for efficient mild-temperature photothermal therapy. *Adv. Sci.* **10**, e2303911 (2023).
14. Zhu, Y. et al. Rational design of biomaterials to potentiate cancer thermal therapy. *Chem. Rev.* **123**, 7326–7378 (2023).
15. Pei, Z., Lei, H. & Cheng, L. Bioactive inorganic nanomaterials for cancer theranostics. *Chem. Soc. Rev.* **52**, 2031–2081 (2023).
16. Cui, X. et al. Photothermal nanomaterials: A powerful light-to-heat converter. *Chem. Rev.* **123**, 6891–6952 (2023).
17. Bayda, S. et al. Inorganic nanoparticles for cancer therapy: aTransition from lab to clinic. *Curr. Med. Chem.* **25**, 4269–4303 (2018).
18. Panwar, N. et al. Nanocarbons for biology and medicine: Sensing, imaging, and drug delivery. *Chem. Rev.* **119**, 9559–9656 (2019).
19. Zhou, L., Dong, K., Chen, Z., Ren, J. & Qu, X. Near-infrared absorbing mesoporous carbon nanoparticle as an intelligent drug carrier for dual-triggered synergistic cancer therapy. *Carbon* **82**, 479–488 (2015).
20. Chen, H. et al. Bright X-ray and up-conversion nanophosphors annealed using encapsulated sintering agents for bioimaging applications. *J. Mater. Chem. B* **5**, 5412–5424 (2017).
21. Yang, M. et al. Upconversion nanotubes with tunable fluorescence properties based on Gd_2O_2S:Ln^{3+} (Ln^{3+} = Yb^{3+}, Er^{3+}) and derivatives for photodynamic therapy. *IET Nanobiotechnol.* **14**, 347–356 (2020).
22. Gao, G. et al. Molecular targeting-mediated mild-temperature photothermal therapy with a smart albumin-based nanodrug. *Small* **15**, e1900501 (2019).
23. Yang, H., Li, C., Tang, J. & Suo, Z. Strong and degradable adhesion of hydrogels. *ACS Appl. Bio. Mater.* **2**, 1781–1786 (2019).
24. Xu, M. et al. An intelligent nanoplatform for imaging-guided photodynamic/photothermal/chemo-therapy based on upconversion nanoparticles and CuS integrated black phosphorus. *Chem. Eng. J.* **382**, 122822 (2020).
25. Xie, J. et al. Single cell sequencing analysis constructed the N7-methylguanosine (m7G)-related prognostic signature in uveal melanoma. *Aging* **15**, 2082–2096 (2023).
26. Zhao, A., Wang, Z., Wang, Y. & Chen, X. Prognostic values of Annexins and validation of the influence on cell proliferation, migration, and invasion in uveal melanoma. *Am. J. Transl. Res.* **15**, 3131–3151 (2023).
27. Sudaka, A. et al. Combination of bevacizumab and irradiation on uveal melanoma: an in vitro and in vivo preclinical study. *Invest. N. Drugs* **31**, 59–65 (2013).
28. Jia, G., Yang, M., Song, Y., You, H. & Zhang, H. General and facile method to prepare uniform Y_2O_3:Eu hollow microspheres. *Cryst. Growth Des.* **9**, 301–307 (2009).
29. Zhou, J. et al. NIR Photothermal therapy using polyaniline nanoparticles. *Biomaterials* **34**, 9584–9592 (2013).
30. Li, L. et al. Pedot nanocomposites mediated dual-modal photodynamic and photothermal targeted sterilization in both NIR I and II window. *J. Biomater.* **41**, 132–140 (2015).
31. Chang, M. et al. Cu_2MoS_4/Au Heterostructures with enhanced catalase-like activity and photoconversion efficiency for primary/metastatic tumors eradication by phototherapy-induced immunotherapy. *Small* **16**, 1907146 (2020).
32. Han, X., Li, H., Zhou, D., Chen, Z. & Gu, Z. Local and targeted delivery of immune checkpoint blockade therapeutics. *Acc. Chem. Res.* **53**, 2521–2533 (2020).
33. Taymouri, S., Varshosaz, J., Hassanzadeh, F., Javanmard, S. H. & Mahzouni, P. Pharmacokinetics, organ toxicity and antitumor activity of docetaxel loaded in folate targeted cholesterol based micelles. *Curr. Drug Deliv.* **13**, 545–556 (2016).
34. Elechalawar, C. et al. Cationic folate-mediated liposomal delivery of bis-arylidene oxindole induces efficient melanoma tumor regression. *Biomater. Sci.* **5**, 1898–1909 (2017).
35. Yu, Z. et al. Role of apoptosis repressor with caspase recruitment domain (ARC) in cancer. *Oncol. Lett.* **18**, 5691–5698 (2019).
36. Mercier, I. et al. ARC, an apoptosis suppressor limited to terminally differentiated cells, is induced in human breast cancer and confers chemo- and radiation-resistance. *Cell Death Differ.* **12**, 682–686 (2005).
37. Yoon, D. et al. AKAP12 induces apoptotic cell death in human fibrosarcoma cells by regulating CDKI-cyclin D1 and caspase-3 activity. *Cancer Lett.* **254**, 111–118 (2007).
38. Liberzon, A. et al. The molecular signatures database (MSigDB) hallmark gene set collection. *Cell Syst.* **1**, 417–425 (2015).
39. Fang, Y. et al. A low-concentration hydrothermal synthesis of biocompatible ordered mesoporous carbon nanospheres with tunable and uniform size. *Angew. Chem. Int. Ed.* **49**, 7987–7991 (2010).
40. Jia, G. et al. Facile synthesis and luminescence of uniform Y_2O_3 hollow spheres by a sacrificial template route. *Inorg. Chem.* **49**, 7721–7725 (2010).
41. Jyotsana, N. et al. Lipid nanoparticle-mediated siRNA delivery for safe targeting of human CML in vivo. *Ann. Hematol.* **98**, 1905–1918 (2019).
42. McGinnis, S. M., Murrow, L. M. & Gartner, Z. J. DoubletFinder: Doublet detection in single-cell RNA sequencing data using artificial nearest neighbors. *Cell Syst.* **8**, 329–337 (2019).
43. Hao, Y. et al. Integrated analysis of multimodal single-cell data. *Cell* **24**, 3573–3587 (2021).
44. Wu, T. et al. Aug clusterProfiler 4.0: A universal enrichment tool for interpreting omics data. *Innovaction* **28**, 100141 (2021).
45. Van de Sande, B. et al. Aerts S A scalable SCENIC workflow for single-cell gene regulatory network analysis. *Nat. Protoc.* **15**, 2247–2276 (2020).
46. Newman, A. M. et al. Determining cell type abundance and expression from bulk tissues with digital cytometry. *Nat. Biotechnol.* **37**, 773–782 (2019).

Acknowledgements

This work was supported in part by the Project of Shanghai Science and Technology (Grant No. 23ZR1409500, M Yang, 23S11900200, M Yang, 23XD1420500, J. Huang), EYE & ENT Hospital of Fudan University High-level Talents Program (Grant No. 2021318, J. Huang), Clinical Research Plan of SHDC (Grant No. SHDC2020CR1043B, X. Zhou), Project of Shanghai Xuhui District Science and Technology (Grant No. 2020-015, X. Zhou), Fund of Fudan University and Cao'ejiang Basic Research (24FCA16, J. Huang), Program for Professor of Special Appointment (Eastern Scholar, TP2022046, J. Huang) at Shanghai Institutions of Higher Learning, Fund of National Key Clinical Specialties Construction Project of Shanghai Municipal Health Commission (Grant No. Z155080000004, X. Zhou), Medical Engineering fund of Fudan University (yg2023-06 and yg2023-26), Shanghai Anticancer Association EYAS PROJECT (SACA-CY22C03, Z. Chen). The funders had no role in study design, data collection and analysis, decision to publish, or reparation of the manuscript.

Author contributions

M. Yang, J. Huang, X. Zhou, and W. Tao conceptually designed the studies. M. Yang, J. Huang, Z. Zeng, and Z. Chen interpreted the results. M. Yang, Y. Huang, Q. Ye, B. Bao, N. Zhao, and X. Chen performed the in vitro materials synthesis and characterization, M Yang analyzed the materials characterization results. Y. Huang, Q. Ye, N. Zhao, Z. Chen, performed in vitro cell biocompatibility evaluation. Y. Huang, Z. Chen, and Q. Ye performed subcutaneous melanoma animal surgeries and collected tissue samples. Z. Chen, Q. Ye, W. Xing, T. Chen, X. Chen, J. Li, Q. Gao, S. Zhang, A. Chen, and H. Xu performed ocular in situ melanoma animal surgeries and collected tissue samples. M. Yang and Z. Chen analyzed the in vivo evaluation results. Z. Zeng and Z. Zhou performed and analyzed the single-cell RNA sequencing analysis. M. Yang drafted

the manuscript with input from all authors. H. Pan and Z. Chen performed the schematic drawing. M. Yang, Z. Zeng, Z. Chen, X. You, and J. Huang edited the manuscript. Y. Xiao polished the manuscript. Y. Li, N. Kong, and W. Tao provided consultation, data evaluation and polish the manuscript. J. Huang, M. Yang, X. Zhou, and Z. Chen obtained the funding. All authors commented on the paper.

Competing interests
The authors declare no competing interests.

Additional information
Supplementary information The online version contains supplementary material available at https://doi.org/10.1038/s41467-025-60454-5.

Correspondence and requests for materials should be addressed to Mei Yang, Wei Tao, Xingtao Zhou or Jinhai Huang.

Peer review information *Nature Communications* thanks the anonymous reviewer(s) for their contribution to the peer review of this work. A peer review file is available.

[1]Eye Institute and Department of Ophthalmology, Eye & ENT Hospital, Fudan University; NHC Key Laboratory of Myopia and Related Eye Diseases, Shanghai, China. [2]Key Laboratory of Myopia and Related Eye Diseases, Chinese Academy of Medical Sciences, Shanghai, China. [3]Shanghai Research Center of Ophthalmology and Optometry, Shanghai, China. [4]School of Ophthalmology and Optometry and Eye Hospital, Wenzhou Medical University, Wenzhou, Zhejiang, China. [5]Center for Nanomedicine and Department of Anesthesiology, Brigham and Women's Hospital, Harvard Medical School, Boston, MA, USA. [6]These authors contributed equally: Mei Yang, Yida Huang, Zhongxing Chen, Qianfang Ye, Zhenhai Zeng, Xinru You. ✉e-mail: meiyang@fudan.edu.cn; wtao@bwh.harvard.edu; xingtaozhou@fudan.edu.cn; jinhaihuang@fudan.edu.cn